Miner Deposita (2015) 50:967–986
DOI 10.1007/s00126-015-0580-5

ARTICLE

Methane origin and oxygen-fugacity evolution of the Baogutu reduced porphyry Cu deposit in the West Junggar terrain, China

Ping Shen · HongDi Pan

Received: 21 March 2013 / Accepted: 19 February 2015 / Published online: 17 March 2015

Abstract Most porphyry copper deposits worldwide contain magnetite, hematite, and anhydrite in equilibrium with hypogene copper-iron sulfides (chalcopyrite, bornite) and have fluid inclusions with CO_2>>CH_4 that are indicative of high fO_2. In contrast, the Baogutu porphyry Cu deposit in the West Junggar terrain (Xinjiang, China) lacks hematite and anhydrite, contains abundant pyrrhotite and ilmenite in equilibrium with copper-iron sulfides (chalcopyrite), and has fluid inclusions with CH_4>>CO_2 that are indicative of low fO_2. The mineralized intrusive phases at Baogutu include the main-stage diorite stock and minor late-stage diorite porphyry dikes. The main-stage stock underwent fractional crystallization and country-rock assimilation-contamination, and consists of dominant diorite and minor gabbro and tonalite porphyry. The country rocks contain organic carbons (0.21–0.79 wt.%). The $\delta^{13}C_{VPDB}$ values of the whole rocks (−23.1 to −25.8‰) in the wall rocks suggest a sedimentary organic carbon source. The $\delta^{13}C_{VPDB}$ values of CH_4 (−28.2 to −36.0‰) and CO_2 (−6.8 to −20.0‰) in fluid inclusions require an organic source of external carbon and equilibration of their $\Delta^{13}C_{CO2\text{-}CH4}$ values (8.2–25.0‰) at elevated temperatures (294–830 °C) suggesting a significant contribution of thermogenic CH_4. Mineral composition data on the main-stage intrusions, such as clinopyroxene, hornblende, biotite, magnetite, ilmenite, sphene, apatite, and pyrrhotite, suggest that the primary magma at Baogutu was oxidized and became reduced after emplacement by contamination with country rocks. Mineral compositions and fluid inclusion gas compositions suggest that the redox state of the system evolved from logfO_2>FMQ+1 in the magma stage, to logfO_2<FMQ as a consequence of country rocks assimilation-contamination, to logfO_2>FMQ in the hydrothermal stage. Though oxidized magma was emplaced initially, assimilation-contamination of carbonaceous country rocks decreased its fO_2 such that exsolved fluids contained abundant CH_4 and deposited a reduced assemblage of minerals.

Keywords Oxygen fugacity · CH_4-rich fluid · Assimilation-contamination · Baogutu reduced porphyry deposit · West Junggar

Editorial handling: G. Beaudoin and T. Wagner

Electronic supplementary material The online version of this article (doi:10.1007/s00126-015-0580-5) contains supplementary material, which is available to authorized users.

P. Shen (✉)
Key Laboratory of Mineral Resources, Institute of Geology & Geophysics, Chinese Academy of Sciences, Beijing 100029, China
e-mail: pshen@mail.iggcas.ac.cn

H. Pan
College of Earth Sciences, Chang'an University, Xi'an 710054, China

Introduction

It is well established that porphyry copper deposits form in association with subduction-related oxidized-type or high-oxygen-fugacity (fO_2) magmas (logfO_2>FMQ+2, where FMQ is the fayalite-magnetite-quartz oxygen buffer, Mungall 2002). Such oxidized magmas are considered to be the source of the metals and S in the ore fluids (Hedenquist and Lowenstern 1994; Cooke et al. 2005; Richards 2003). Hence, these porphyry deposits are characterized by high fO_2 minerals (e.g., magnetite, hematite, and anhydrite) in equilibrium with hypogene copper-iron sulfide minerals (chalcopyrite, bornite) and hydrothermal fluids with CO_2>>CH_4 (Kirkham and Sinclair 1995; Mungall 2002; Cooke et al. 2005).

Though many deposits have these characteristics, there is increasing evidence for the existence of some porphyry Cu-Au deposits that have CH_4-rich hydrothermal fluids and abundant hypogene pyrrhotite, but lack primary high fO_2 minerals

(e.g., magnetite, hematite, and anhydrite), such as at the 17 Mile Hill and Boddington deposits in Western Australia and the Madeleine, Rosslan, and Catface deposits in Canada (Rowins 1999, 2000; Smith et al. 2012). The Baogutu porphyry Cu deposit, located in the West Junggar terrain (Xinjiang, NW China), has pyrrhotite in equilibrium with copper-iron-arsenic sulfides (chalcopyrite, pyrite, arsenopyrite) and substantial CH_4 in ore fluids (Shen et al. 2010a, b). The mineralized diorite contains primary magnetite. The Baogutu is a reduced porphyry Cu deposit (Shen et al. 2011; Shen and Pan 2013) according to Rowins' (2000) classification. This study shows further that primary ilmenite, sphene, and pyrrhotite are present in the Baogutu deposit. In addition, we also discovered that several other porphyry deposits in Xinjiang, NW China, such as the Suyunhe Mo-W, Hongyuan Mo and Tuketuke Cu-Mo deposits in West Junggar (Fig. 1b), and the Yandong Cu deposit in the East Tianshan Mountains, contain substantial CH_4 in ore fluids. Moreover, the Lailisigaoer and Lamasu porphyry-skarn Cu-Mo deposits in the West Tianshan Mountains (Xinjiang, NW China) and the Taipingchuan porphyry Cu-Mo deposit in Inner Mongolia (NE China) have CH_4-rich inclusions (Zhu et al. 2012). Such CH_4-rich fluids may be widespread in the porphyry Cu deposits of North China in the Central Asian Orogenic Belt (CAOB).

Previous researchers (Ague and Brimhall 1988; Rowins 1999, 2000; Smith et al. 2012) proposed that these deposits are formed in association with ilmenite-bearing, reduced I-type granitoids and relatively reduced hydrothermal fluids, i.e., at fO_2 values below FMQ. However, it is generally accepted that oxidized magmas promote the oxidation of residual sulfide in the mantle wedge and consequent liberation of chalcophile elements (e.g., Mungall 2002; Richards 2003; Cooke et al. 2005; Sillitoe 2010). It is therefore important to determine whether or not the magmas in these systems were reduced or oxidized to begin with, the source of the CH_4-rich fluids within them, and the cause of the low oxygen-fugacity conditions evident in these porphyry copper deposits.

Herein we take the Baogutu porphyry Cu deposit as an example and study its petrography, mineral chemistry, fluid inclusion gas, and carbon isotopic compositions in an attempt to (1) determine the source of the CH_4-rich hydrothermal fluids, (2) constrain the oxygen fugacity (fO_2) of the magmas and hydrothermal fluids, and (3) decipher the origin of the reducing conditions in this deposit. This information is important in the ongoing efforts to understand the range of processes that produce large porphyry copper deposits worldwide.

Geologic setting of the Baogutu deposit

The West Junggar terrain, located in the center of the CAOB (Fig. 1a), is largely comprised of Paleozoic volcanic arcs in the north and accretionary complexes in the south (e.g., Xiao et al. 2008; Shen et al. 2012a, 2014). They were accreted onto the Kazakhstan plate as the Tarim, Kazakhstan, and Siberian plates converged (Xiao et al. 2008). The Baogutu porphyry Cu deposit is located in the Carboniferous Kelamay arc in the south-western part of the terrain (Fig. 1b).

Fig. 1 **a** Schematic map of the Central Asian Orogenic Belt (Shen et al. 2010a) showing principal porphyry Cu deposits (*1* Baogutu, *2* Tuwuyandong, *3* Wunuhetushan, *4* Duobaoshan, *5* Erdenet, *6* Tsagaan-Suvarga, *7* Oyu Tolgoi, *8* Bozshakol, *9* Nurkazghan, *10* Borly, *11* Kounrad, *12* Sayak, *13* Aktogai, *14* Koksai, *15* Taldy Bulak, *16* Kal'makyr). **b** Geological map of the West Junggar, showing principal Cu, Au, and W-Mo deposits

The Baogutu porphyry Cu deposit has resources of 225 Mt of ore at 0.28 wt.% Cu, 0.01 wt.% Mo, and 0.14 g/t Au (Shen et al. 2010a). Our previous work has recognized two mineralized intrusive phases at Baogutu (Shen et al. 2010a, b): the main-stage (Stage 1) diorite stock and minor late-stage (Stage 2) diorite porphyry dikes (Fig. 2, Table 1). The composition and occurrence of the main-stage stock varies significantly (Shen and Pan 2013). For example, the main-stage stock has a wide compositional range from very minor gabbro (Fig. 3a) through dominant diorite (Fig. 3b) to minor tonalite porphyry (Fig. 3c). These rocks are heterogeneous over a few to dozens of meters (Fig. 2b). Some felsic micro-granular xenoliths and heterogeneous phenocrysts occur in these rocks. The $\varepsilon Nd(t)$ values of these rocks range from 3.2 to 6.0 (Shen and Pan 2013). The character of the elemental and Sr-Nd geochemistry of the tonalite porphyry is between the diorite and the country rocks. The main-stage stock underwent country-rock assimilation-contamination and the greatest amount of assimilation occurred during crystallization of the tonalite porphyry (Shen and Pan 2013). The gabbro, diorite, and tonalite porphyries occur in an island arc (Shen et al. 2009; Shen and Pan 2013).

The main-stage diorite stock and late-stage diorite porphyry dike formed the Baogutu complex which intruded the Lower Carboniferous Baogutu and Xibeikulasi Groups. The Baogutu Group includes tuffaceous siltstone, silty tuff, and felsic tuff with intercalations of andesite and pebbly greywacke and lenses of limestone, marl, and bioclastic limestone. The Xibeikulasi Group consists of greywacke with graded bedding, tuffaceous mudstone, and tuffaceous siltstone (Shen et al. 2013). Some carbon-bearing rocks such as argillaceous silty tuff, argillaceous siliceous rocks, and argillaceous greywacke (Fig. 3d–f) occurred in the Baogutu and Xibeikulasi Groups.

Main-stage host rocks underwent strong hydrothermal alteration and host the bulk of the Cu-Mo-Au mineralization at Baogutu. Mineralization at Baogutu is dominantly disseminated with lesser stockwork veins and hydrothermal breccia. Sulfides are chalcopyrite, pyrite, and pyrrhotite, followed by minor arsenopyrite and molybdenite and rare sphalerite and galena.

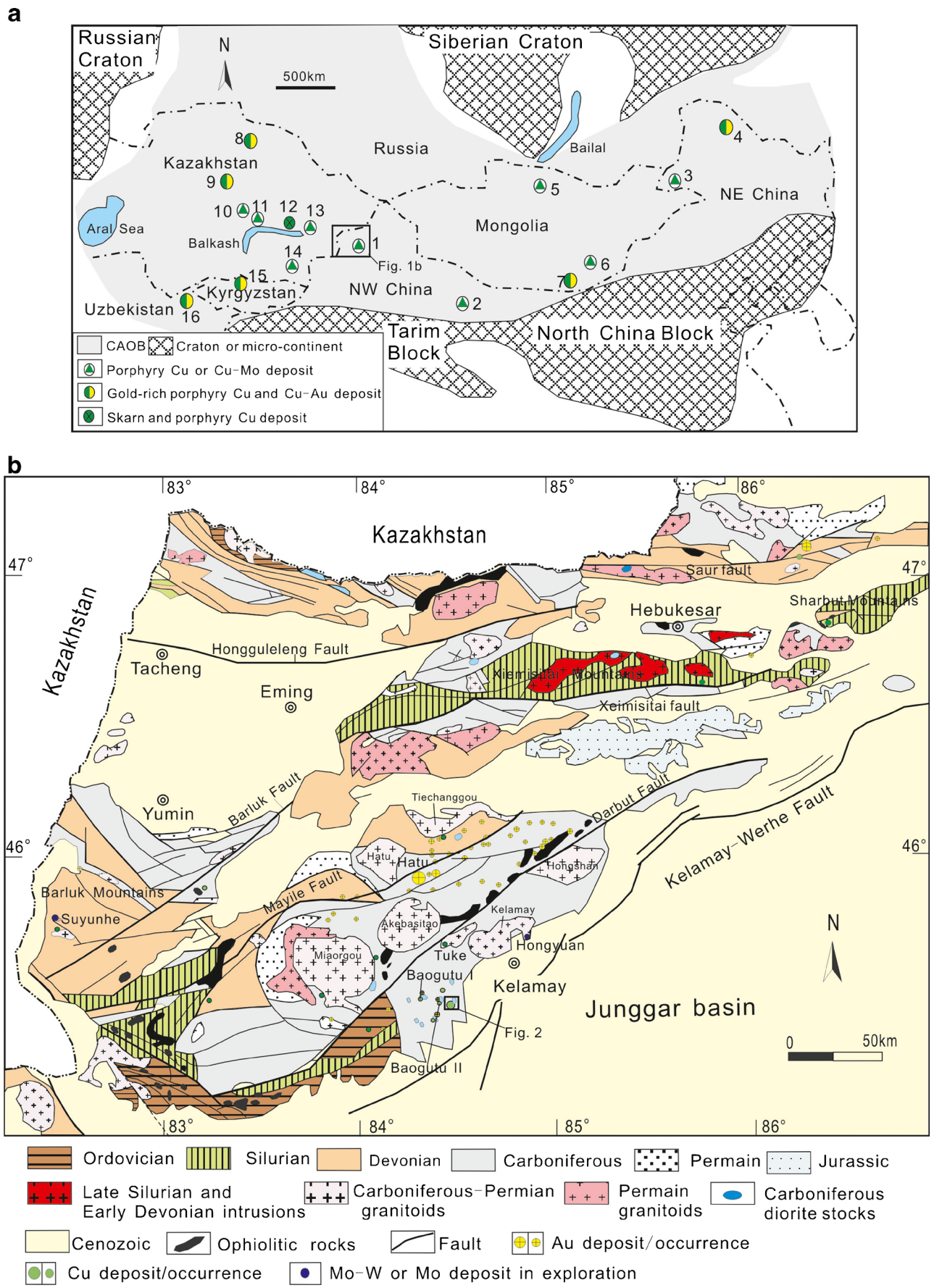
a
Russian Craton
N
500km
Siberian Craton
Russia
Bailal
Kazakhstan
8
9
4
3
5
NE China
10
11
12
13
Aral Sea
Balkash
Mongolia
1
Fig. 1b
14
6
15
Kyrgyzstan
NW China
7
Uzbekistan
16
2
Tarim Block
North China Block
CAOB
Craton or micro-continent
Porphyry Cu or Cu-Mo deposit
Gold-rich porphyry Cu and Cu-Au deposit
Skarn and porphyry Cu deposit
b
83°
84°
85°
86°
Kazakhstan
47°
Saur fault
Sharbut Mountains
Hebukesar
Kazakhstan
Hongguleleng Fault
Tacheng
Eming
Xiemisitai Mountains
Xeimisitai fault
Barluk Fault
Yumin
Tiechanggou
Darbut Fault
Kelamay-Werhe Fault
46°
Hatu
Hongshan
Barluk Mountains
Mayile Fault
Suyunhe
Akebasitao
Kelamay
Miaorgou
Tuke
Hongyuan
Baogutu I
Kelamay
Junggar basin
N
Fig. 2
0
50km
Baogutu II
Ordovician
Silurian
Devonian
Carboniferous
Permain
Jurassic
Late Silurian and Early Devonian intrusions
Carboniferous-Permian granitoids
Permain granitoids
Carboniferous diorite stocks
Cenozoic
Ophiolitic rocks
Fault
Au deposit/occurrence
Cu deposit/occurrence
Mo-W or Mo deposit in exploration

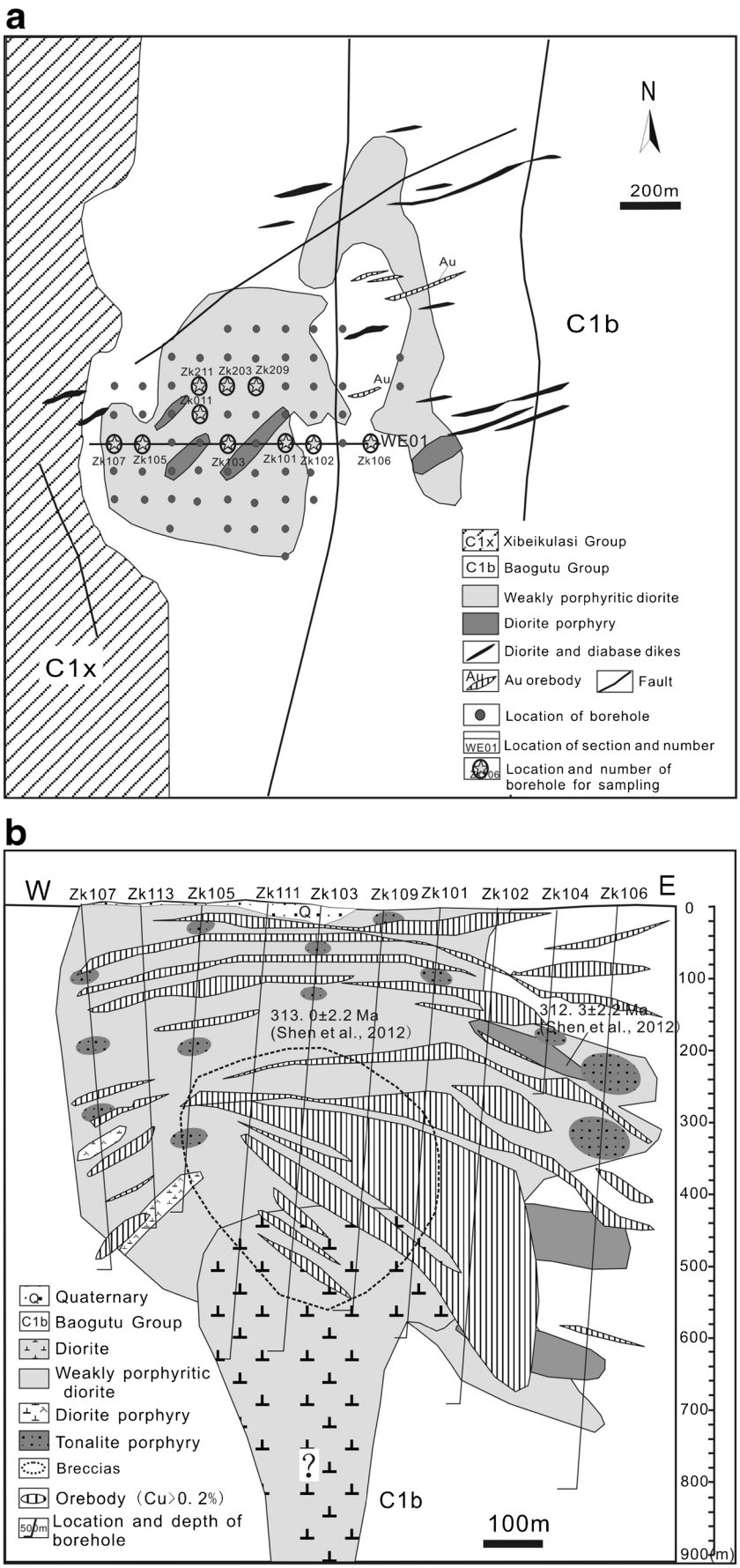

Fig. 2 **a** Geological map of the Baogutu deposit. Line WE01 shows the location of the section shown in (**b**). **b** Geologic cross-section along WE01 (Shen and Pan 2013)

Table 1 Summary description of the Baogutu complex and associated alteration, mineralization, and fluid system

Stage	Sub-stage	Rocks/alterations	Main minerals	Minor minerals	Vein style	Fluid system	This study
Magma emplacement	Magma stage 1	Rare gabbro	Plagioclase, hornblende	Pyroxene, biotite, magnetite, ilmenite, sphene		H_2O+minor CO_2	Not used
		Dominant granular to weakly porphyritic diorite	Plagioclase, hornblende, biotite	Quartz, magnetite, ilmenite, sphene		H_2O+minor CO_2	Used
	Assimilated stage	Minor tonalite porphyry	Plagioclase, biotite, quartz	Hornblende, apatite		H_2O-CO_2+minor CH_4	Used
Alteration	Stage 1A	Barren Ca-Na silicate alteration	Actinolite, albite, epidote	Pyrrhotite, apatite	A-type vein: Apa-Qtz, Bi-Qtz veinlets	H_2O-CH_4	Used
	Stage 1B	Potassic alteration	Biotite, quartz	Rutile, sphene, chlorite	Qtz-Cpy-Py, Qtz-Cpy-Py-Mo, Qtz-Cpy-Py, Pyr-Qtz veinlets	H_2O-CH_4-CO_2	Used
	Stage 1C	Phyllic alteration	Quartz, sericite	Chlorite	Qtz-Mo-Cpy, Qtz-Cpy-Py, Pyr-Qtz veinlets	H_2O-CO_2-CH_4	Used
Magma emplacement	Magma stage 2	Diorite porphyry	Plagioclase, hornblende, biotite	Quartz		Undetected	Not used
Alteration	Stage 2B	Potassic alteration	Biotite		Qtz-Cc, Qtz-Cc-Bi-Cpy-Py	Undetected	Not used

Apa apatite, *Bt* biotite, *Cc* calcite, *Cpy* chalcopyrite, *Mo* molybdenite, *Pyr* pyrrhotite, *Py* pyrite, *Qtz* quartz

Three alteration sub-stages are recognized in the main-stage host rocks based on our previous work (Shen et al. 2010a, b) and this study (Table 1). Stage 1A is the barren Ca-Na silicate alteration stage, which produced secondary actinolite, albite, and epidote. Only remnants of the earliest Ca-Na silicate alteration assemblage are preserved in the diorite. Stage 1B consists of extensive potassic (biotite) and propylitic alteration, which formed the inner potassic alteration zone and outer propylitic alteration zone. The dominant disseminated mineralization and minor quartz-sulfide veins and hydrothermal breccia occur in the inner potassic alteration zone. Potassic alteration is associated with most of the Cu-Au mineralization. Stage 1C consists of phyllic alteration (sericite-quartz±chlorite) and where associated hydrothermal veins overprint Stage 1B. Phyllic alteration is associated with most of the Cu-Mo mineralization.

Our previous work (Shen et al. 2010b) showed that most inclusions in quartz, from all alteration sub-stages (Stage 1A, 1B, and 1C), are rich in CH_4 and H_2O with minor CO_2 (Table 1); Stages 1A and 1B contain halite and sylvite but lack high fO_2 minerals (e.g., magnetite, hematite, and anhydrite). We estimated fluid trapping conditions at T >400 °C and P= 1500 to 3100 bar (depth=5–10 km) in Stage 1A, T=200 to 400 °C and P=50 to 320 bar (depth<3.2 km) in Stage 1B, and T=170 to 400 °C and P=20 to 230 bar (depth<2.3 km) in Stage 1C.

The SIMS (secondary ion mass spectrometry) zircon U-Pb ages of the main-stage diorites and late-stage diorite porphyry are 313.0±2.2 and 312.3±2.2 Ma, respectively (Shen et al. 2012b). Molybdenite, formed in the main stage, yielded an Re-Os mean model age of 310±3.6 Ma (Song et al. 2007) and 312.4±1.8 Ma (Shen et al. 2012b).

Analytical methods

Samples used in the study were collected from eight diamond drill holes (Fig. 2a) within the least altered diorite and hypogene alteration zones (phyllic and potassic) from the main-stage stock (Table 1). Some samples of the wall rocks of the Baogutu group were also selected from the area near to the Baogutu intrusion. Over 200 polished thin sections were studied using transmitted and reflected light microscopy. Analyses were undertaken at the Institute of Geology and Geophysics, Chinese Academy of Sciences, Beijing.

Whole-rock major element analysis

About ten host rocks and five carbon-bearing wall rocks at Baogutu were selected for whole-rock major element analysis. Major elements were determined by x-ray fluorescence (Shimadzu XRF-1700/1500) after fusion with lithium tetraborate using Chinese national standard sample

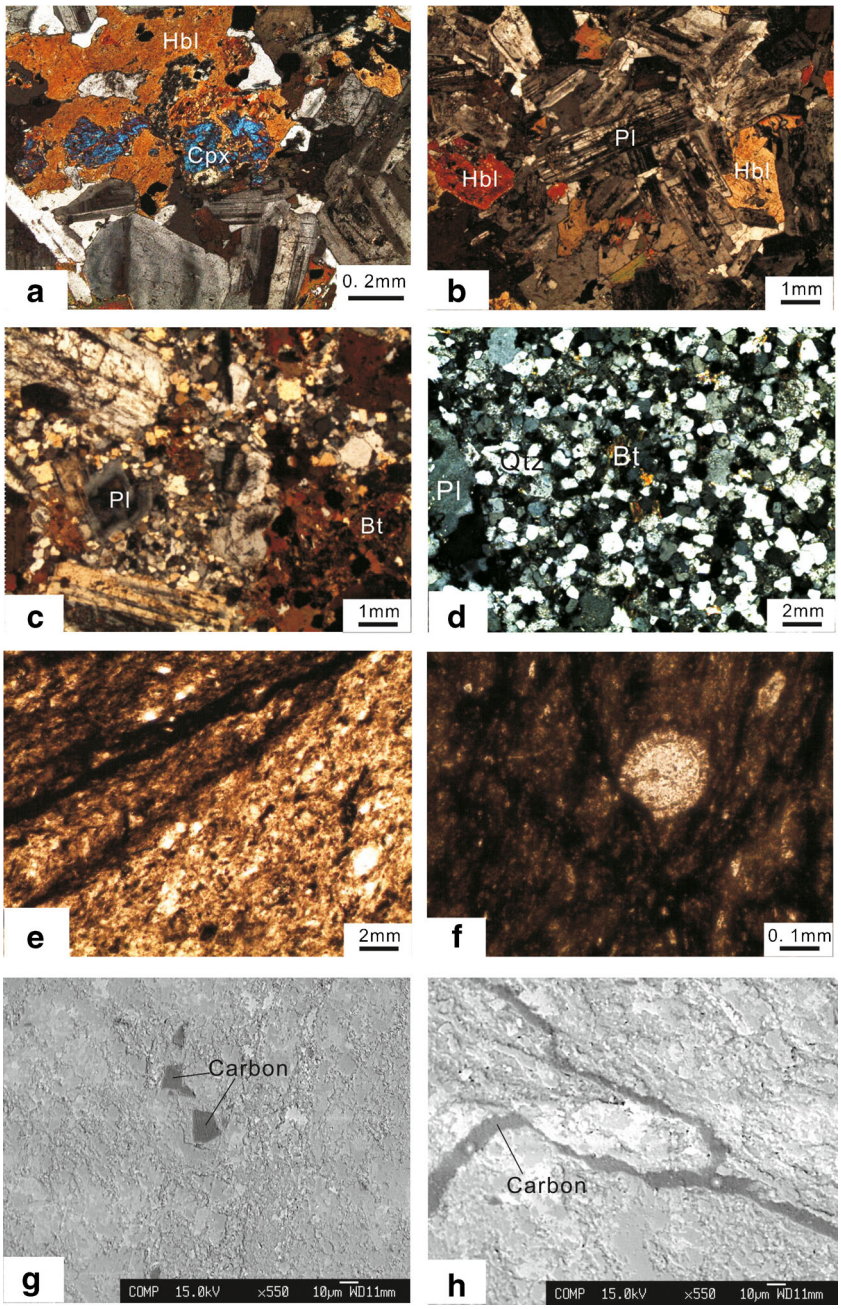

Fig. 3 **a** Gabbro; **b** diorite; **c** assimilated diorite or tonalite porphyry; **d** greywacke; **e** carbon-bearing argillaceous silty tuff; **f** carbon-bearing argillaceous siliceous rocks, showing sponge-spicule fossil; **g** back-scattered electron (BSE) images of siliceous rocks, showing carbon material grains; **h** BSE images of siliceous rocks, showing carbon material veinlets. *Cpx* clinopyroxene, *Hbl* hornblende, *Bt* biotite, *Pl* plagioclase, *Qz* quartz, *Or* K-feldspar, *Mt* magnetite, *Ilm* ilmenite, *Rt* rutile, *Cpy* chalcopyrite, *Py* pyrite, *Po* pyrrhotite, *Apa* apatite, *Sph* sphene

GBW07101-07114. The precision was better than 1 wt.% in the analysis range. Loss on ignition was measured as weight loss of the samples after 1 h baking at a constant temperature of 1000 °C [Electronic supplementary materials (ESM) 1, 2].

Whole-rock carbon isotopes and organic carbon contents

Ten carbon-bearing rocks of the Baogutu Group in the Baogutu area were selected for chemical analyses. The carbon isotopic compositions of four whole-rock samples were determined on a MAT253 isotope ratio mass spectrometer by conventional off-line methods using pure phosphoric acid. Isotope compositions are expressed as $\delta^{13}C$ relative to VPDB (Table 2). Analytical uncertainties for C isotope compositions are all better than ±0.2‰. Ten whole-rock total carbon contents were determined by high-temperature combustion using an elemental analyzer (EA3000, Leeman Company). Organic carbon contents were determined on splits of each sample that were subjected to multiple acid treatments, including exposure to concentrated HCl fumes followed by additions of 10 % aqueous HCl. These treatments were undertaken on pre-weighed samples in silver holders,

Table 2 Carbon contents (wt.%) and C isotopic data of wall rocks from the Baogutu group

Samples	Rocks	Organic carbon	Inorganic carbon	$\delta^{13}C$
ZZK4-1-7	Argillaceous silt tuff	0.41	0.14	−25.8
ZZK4-1-14	Tuffaceous siltstone	0.49	0.16	−23.1
ZZK4-4-21	Argillaceous siliceous rock	0.47	1.2	
ZZK4-4-27	Tuffaceous siltstone	0.42	0.31	−25.2
ZZK4-4-30	Argillaceous siliceous rock	0.62	1.43	−25.8
BT21-3	Argillaceous silt tuff	0.24	0.6	
BT22-3	Argillaceous silt tuff	0.79	0.48	
BT50-3	Argillaceous silt tuff	0.21	0.45	
BT51-1	Greywacke	0.28	0.21	
BT52-2	Greywacke	0.58	0.16	

which, after oven drying, were wrapped in tin holders and analyzed by high-temperature combustion using the elemental analyzer. Inorganic carbon contents were determined as the difference between the total carbon and organic carbon contents (Table 2).

Electron probe microanalyzer (EPMA)

Three polished thin sections (including the argillaceous silty tuff and argillaceous siliceous rock) were studied by EPMA. Polished thin sections were coated with gold rather than carbon for analysis. Back-scattered electron (BSE) images and the chemical compositions of the materials were acquired using a JXA-8100 with a voltage of 15 kV, a beam current of 20 nA, and a spot size of 1–3 μm.

More than 20 polished thin sections (including the least- and strongly altered rocks) were studied using EMPA. They were coated with carbon for analysis. BSE images and the chemical compositions of clinopyroxene, hornblende, biotite, magnetite, ilmenite, sphene, and apatite were acquired using the same JXA-8100 under the same analytical condition. The sulfide compositions were analyzed using a Cameca SX-51 with a voltage of 20 kV, a beam current of 15 nA, and a spot size of 1 μm. Representative mineral analyses from these minerals are given in ESM 3–13.

Laser Raman spectroscopy

Twelve samples of diorite with various vein types from various depths were collected for analyses. The shape, size, and phase content of fluid inclusions within the quartz crystals were examined under a microscope. Most inclusions analyzed in this study were between 4 and 6 μm in diameter. The gas species in single inclusions were analyzed using a Renishaw 1000 Raman micro-spectrometer according to Burke's (2001) method. A laser beam with a wavelength of 514.5 nm and a spot size of about 1 μm was focused on the bubble in each fluid inclusion using a transmitted light microscope. Peak areas for CO_2, CH_4, and H_2O at about 1281 and 1386 cm^{-1}, 2914–2916 cm^{-1}, and 3500 cm^{-1}, respectively, were used to calculate fluid compositions.

Quadrupole mass spectrometry

Bulk analyses of gas extracted from 12 samples of vein quartz were conducted using a Prisma™ QMS200 quadrupole mass spectrometer. Samples weighing 50 mg were washed, dried, and put in a clean quartz tube on the vacuum inlet system. Samples were baked at 100 °C to remove adsorbed gases on the mineral surfaces. When the pressure in the quartz tube was less than 6×10^{-6} Pa, samples were heated to 550 °C at a rate of 1 °C/3 s. Details of the analytical procedures can be found in Zhu and Wang (2000). The results are given in Table 3.

Stable isotope mass spectrometry

To determine the source of carbon in the fluid inclusions, the carbon isotopic compositions of the extracted CH_4 and CO_2 in the fluid inclusions of 11 quartz samples were determined. Fluid components were extracted from fluid inclusions in the quartz by heating the sample under vacuum at 600 °C for 15 min and passed through a dry ice+ethanol cold trap under vacuum to remove H_2O. The mixed gases passed through a liquid N_2 cold trap to freeze CO_2 that was then collected by heating. The remaining gases (CH_4+N_2) were also sampled and then oxidized by reaction with CuO at 780 °C. The reacted gases (CO_2+H_2O+N_2) passed through a dry ice+ethanol cold trap and then a liquid N_2 cold trap under vacuum to obtain pure CO_2. Both pure CO_2 gases representing the CO_2 and CH_4 carbon composition of fluid inclusions were analyzed on a Finnigan Delta S mass spectrometer. Isotope compositions are expressed as $\delta^{13}C_{CO2}$ and $\delta^{13}C_{CH4}$ relative to VPDB. The analytical uncertainties for the C isotope compositions are all better than ±0.2‰. For more on the experimental procedures, see Li et al. (2014).

Results

Whole-rock geochemistry

Samples of the host rocks from the Baogutu main-stage stock show a large compositional variation, with SiO_2 contents ranging from 53 to 66 wt.%. These SiO_2 contents confirm the petrographic identification of the lithology of ore-hosting rocks: diorite and tonalite porphyry (ESM 1).

The wall rocks at the Baogutu area have high SiO_2 contents ranging from 60 to 74 wt.%. They are felsic tuff, argillaceous silty tuff, argillaceous siliceous rock, and greywacke (ESM 2).

Table 3 Gaseous composition (mol%) and C isotopic data of CH_4 and CO_2 of fluid inclusions from the mineralized quartz at Baogutu

Sample	Veins	Stages	H_2O	N_2	Ar	CO_2	CH_4	C_2H_6	H_2S	CH_4/C_2H_6	$\delta^{13}C_{CH4}$	$\delta^{13}C_{CO2}$	$\delta^{13}C_{CO2\text{-}CH4}$	Equilibrium temperature (°C)
ZK104-90	Qtz-Cpy-(Py) vein	Stage 1B	87.31	0.12	0.03	6.29	6.15	0.09	–	68	−28.4	−11.8	16.6	464
ZK211-413	Qtz-Cpy veinlet	Stage 1B	87.12	0.57	0.04	7.99	4.22	0.06	–	70	−34.7	−14.0	20.7	374
ZK211-276	Qtz-Cpy-Py veinlet	Stage 1B	87.50	0.53	0.12	6.40	5.06	0.36	0.024	14	−29.0	−12.7	15.3	500
ZK102-458[a]	Qtz-Cpy-(Py) vein	Stage 1B	82.12	1.14	0.13	3.49	12.89	0.22	0.04	59	−28.7	−19.6	9.1	774
ZK211-424	Qtz-Cpy-Py veinlet	Stage 1B	84.21	0.05	0.05	10.61	4.17	0.90	0.008	5	−30.7	−10.3	20.4	370
ZK211-262	Qtz-Cpy-Py veinlet	Stage 1B	87.03	0.43	0.04	7.97	4.28	0.23	0.029	19	−31.8	−7.9	23.8	310
ZK106-456	Qtz-Cpy-Py veinlet	Stage 1B	85.15	0.39	0.02	6.92	7.34	0.16	0.017	46	−31.8	−6.8	25.0	294
ZK106-188	Qtz-Cpy-Py veinlet	Stage 1B	86.57	0.29	0.02	8.51	4.45	0.11	0.032	40	−31.6	–		
ZK102-274	Qtz-Cpy-Py vein	Stage 1C	79.56	0.98	0.36	12.53	4.57	1.99	0.004	2	−28.2	−20.0	8.2	830
ZK203-490	Qtz-Mo vein	Stage 1C	78.53	1.55	0.31	11.29	8.05	0.29	0.01	28	−32.4	−17.1	15.3	500
ZK211-508	Qtz-Mo-Cpy vein	Stage 1C	79.53	2.05	0.02	9.43	8.04	0.92	0.006	9	−34.2	−10.7	23.5	316
ZK211-395	Qtz-Mo-Cpy vein	Stage 1C	78.92	1.71	0.04	6.08	12.80	0.45	0.002	28	−36.0	–		
ZK211-427	Qtz-Mo-Cpy vein	Stage 1C	87.74	0.41	0.02	8.55	3.16	0.12	–	26	−30.8	–		

Equilibrium temperature values according to Horita (2001)

Cpy chalcopyrite, *Mo* molybdenite, *Py* pyrite, *Qtz* quartz, − not detected

[a] Gas composition from Shen et al. (2010b)

Petrography of the host rocks

Our previous work gives a petrographic description of the Baogutu host rocks and associated alteration and mineralization (Shen et al. 2010a, b; Shen and Pan 2013). Important features, for this study, in the main-stage diorite stock at Baogutu are outlined here.

Primary iron-titanium oxides (magnetite, ilmenite) and sphene occur in the diorites from the Baogutu main-stage stock (Fig. 4a–c). Primary magnetite-ilmenite has exsolution textures (Fig. 4a), suggesting that they formed in the late magma stage. Primary sphene is included in biotite and plagioclase (Fig. 4c).

Hornblende is intergrown with plagioclase (Fig. 3b), which indicates that it began crystallizing relatively early. Petrographic textures of biotite indicate that it began crystallizing early in the diorite and tonalite porphyry. Primary biotite from these rocks contains inclusions of primary apatite (Fig. 4d). Some apatite occurs in the groundmass of the tonalite porphyry (Fig. 4e) and contains external fine-grained materials (biotite and quartz; Fig. 4f).

Primary pyrrhotite in diorite (Fig. 4i, j) shows interstitial shape between plagioclase. The interstitial pyrrhotite implies that it formed soon after consolidation of the Baogutu diorite melt, during the transition from magmatic to hydrothermal stage.

Based on the classification of Gustafson and Hunt (1975) and Dilles and Einaudi (1992), A-type veins (Fig. 4k, l) formed in the late magma stage or earliest Stage 1A. The apatite-quartz veinlet occurred in the top of the main-stage stock; the boitite veinlet and K-feldspar-quartz veinlet occurred in the wall rocks. They are characterized by an irregular discontinuous structure (Fig. 4k, l) and suggest fracturing of a plastic rather than a brittle rock. Secondary Ti-bearing minerals (rutile and sphene) occur in the potassic zone during Stage 1B and coexist with secondary biotite (Fig. 5a–c).

Mineral composition of the host rocks

Our previous work has reported the compositions of primary clinopyroxene, plagioclase, hornblende, and biotite in the gabbro, diorite, and tonalite porphyry (Shen and Pan 2013). In this study, the compositions of new primary clinopyroxene, hornblende, and biotite in the diorite were determined by EMPA. The compositions of magnetite, ilmenite, sphene, and apatite in the diorite and secondary biotite in potassically altered diorite were also determined by EMPA.

Clinopyroxene from the diorite is compositionally variable and ranges from diopside-rich to diopside-poor varieties (Fig. 6a) with Mg# values [$Mg/(Mg+Fe^{2+})$] ranging from 0.58 to 0.83 (ESM 3).

Primary brown hornblende from the diorite plots the Mg-hornblende field (Fig. 6b) of Leake (1997). Their Mg# values are high (0.72–0.81) and homogeneous (ESM 4).

Both primary and hydrothermal biotites (ESMs 5, 6) from the diorites are classified as Mg-biotites (Fig. 6c; Foster 1960). Primary biotite chemical compositions are characterized by high TiO_2 (3.11–4.23 wt.%) and Mg# values (0.51–0.61; ESM 5). Hydrothermal biotites have low TiO_2 (0.93–

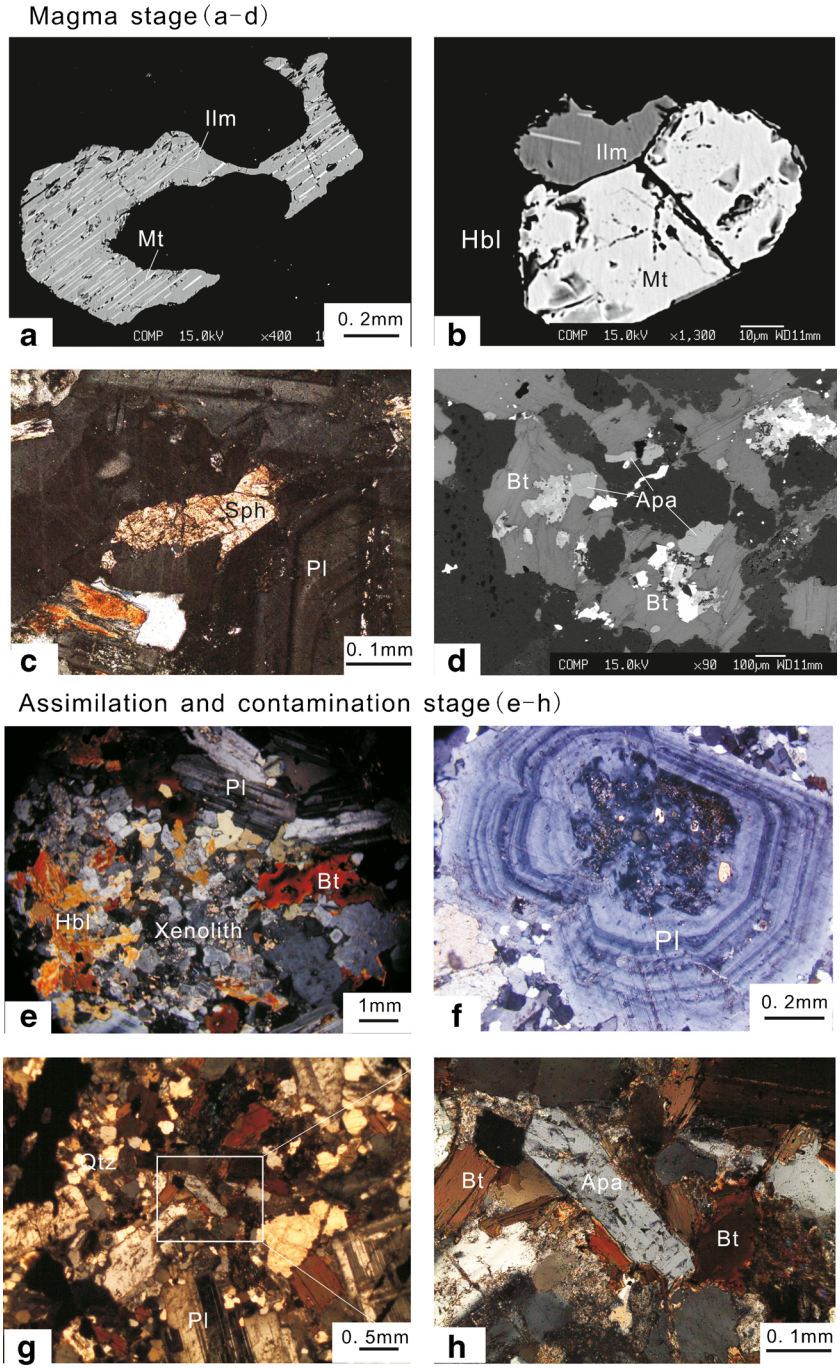

Fig. 4 Photomicrographs and back-scattered electron (BSE) images of the main-stage stock. Magma stage: **a** ilmenite BSE image in (**a**), showing ilmenite-magnetite intergrowths; **b** BSE image, showing coexistence of ilmenite and magnetite with eutectic point; **c** diorite, plagioclases contains sphene; **d** diorite BSE image, biotite contains apatite. Assimilation stage: **e** xenolith in diorite, xenolith consists of felsic fragments; **f** plagioclase contains heterogeneous cores and zoned mantle; **g**, **h** tonalite porphyry, showing heterogeneous apatite. Late-magma stage or Stage 1A: **i** interstitial pyrrhotite between plagioclase in the diorite (under plane light); **j** BSE image showing interstitial pyrrhotite in the diorite; **k** A-type vein, apatite-quartz veinlets; **l** A-type vein, K-feldspar-quartz veinlets. Abbreviations are as in Fig. 3

1.39 wt.%) and high Mg# values (0.67–0.76; ESM 6). All biotites have low halogen contents and contain 0.04 to 1.07 wt.% F and 0.07 to 0.43 wt.% Cl (ESMs 4, 5).

According to the Ti-Fe oxide classification of Buddington and Lindsley (1964), all magnetites are transitional between magnetite (Fe_3O_4) to hematite (Fe_2O_3) with high Fe_2O_3 (67–68 %) and low FeO (31 %) contents (ESM 7, Fig. 6e). Ilmenites are close to the $FeTiO_3$ end member with high TiO_2 (48–50 %) and FeO (40–43 %) contents and low Fe_2O_3 (4–7 %) contents (ESM 8, Fig. 6e).

Primary sphene in the diorite coexists with plagioclases (ESM 9). Secondary Ti-bearing minerals (rutile

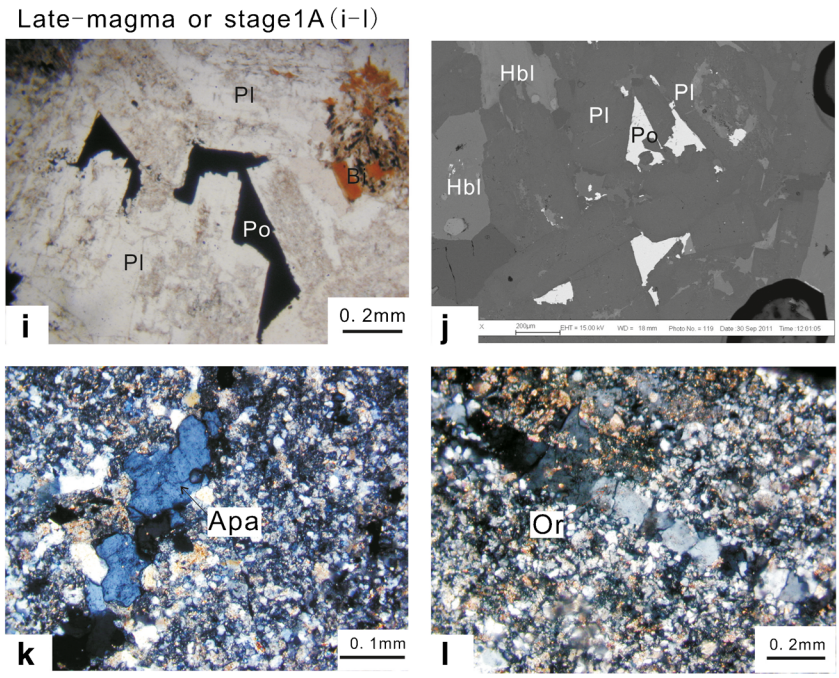

Fig. 4 (continued)

and sphene) occurred in the potassic zone during Stage 1B. Fine-grained Ti-bearing minerals coexist with secondary biotites (Fig. 5a), while large Ti-bearing minerals were probably derived from ilmenite breakdown during hydrothermal alteration (Fig. 5b, c; Rabbia et al. 2009). Compared with primary ilmenite, relict ilmenite is Ti-rich

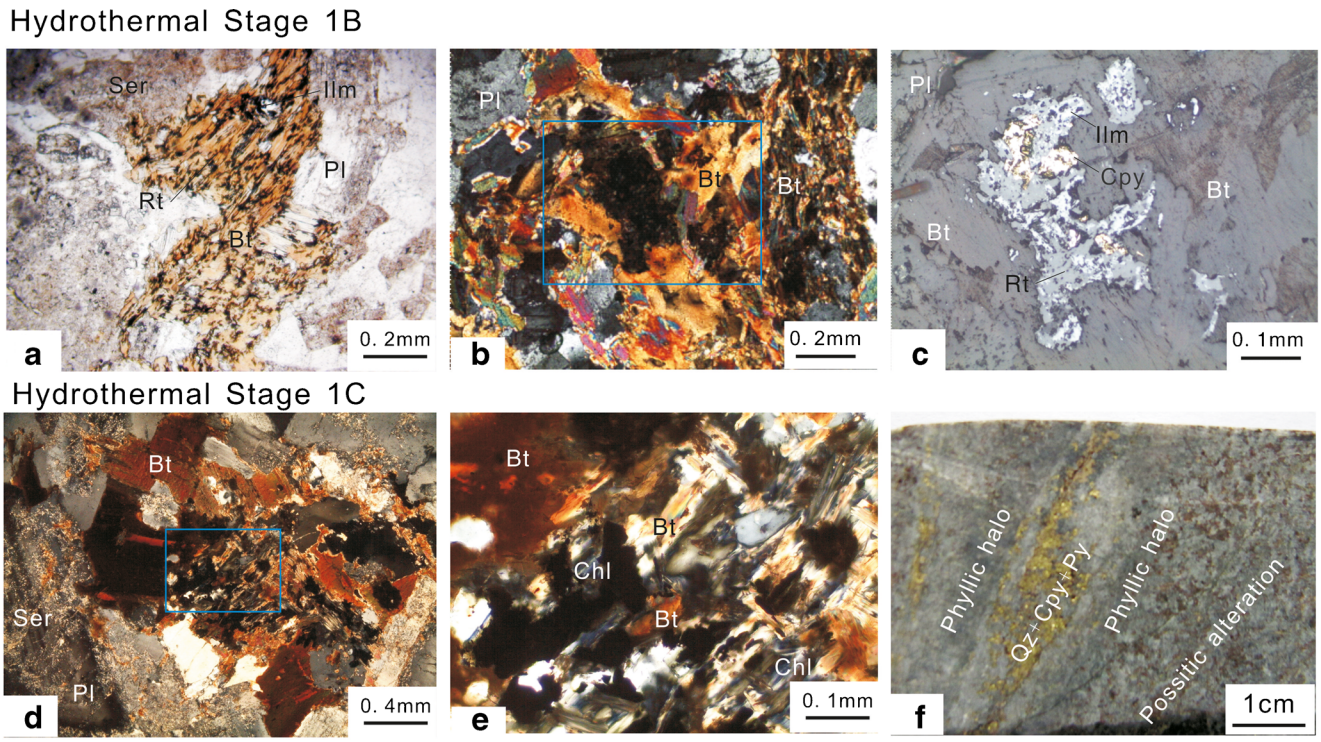

Fig. 5 Photomicrographs and photos of the main-stage diorite stock. Stage 1B: **a** alteration assemblage of Bt+Rt+Ilm in potassic zone; **b** alteration assemblage of Bt+Rt+Ilm+Cpy in potassic zone; **c** enlarged image of (**b**), magmatic ilmenite breakdown showing patches of rutile, sphene, and relictic ilmenite. Stage 1C: **d** alteration assemblage of Ser(sericite)+Chl(chlorite) in phyllic zone; **e** enlarged image of (**d**); **f** Qz+Cpy+Py veinlets with phyllic halo cut the potassic zone. Abbreviations are the same as in Fig. 3

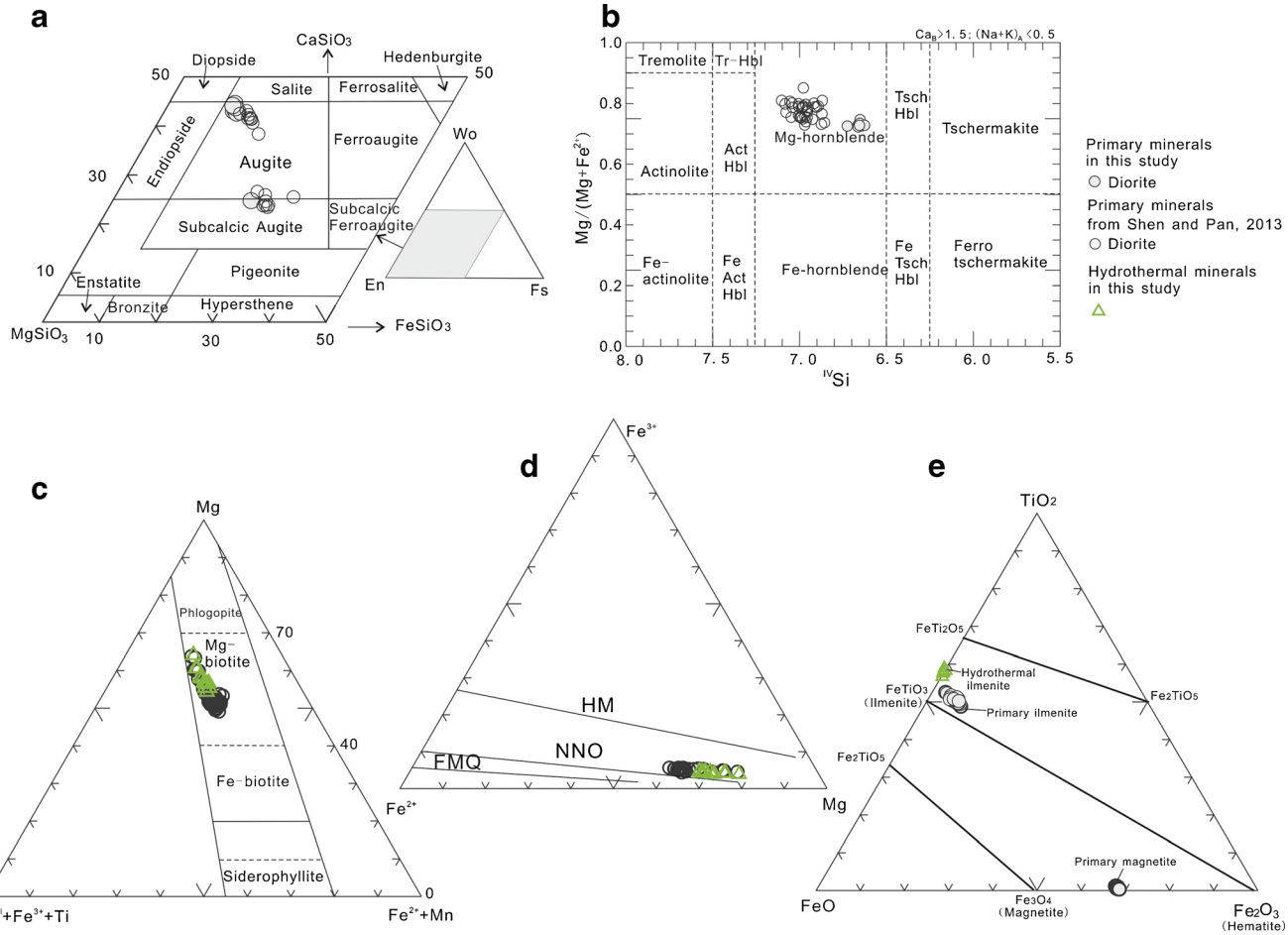

Fig. 6 **a** $CaSiO_3$-$MgSiO_3$-$FeSiO_3$ diagram, showing the compositions of pyroxene in the diorite (Morimoto et al. 1988); **b** classification of amphibole in terms of Si vs. $Mg/Mg+Fe^{2+}$ (Leake 1997); **c** Mg-R^{3+}(Al^{VI}+Fe^{3+}+Ti)-(Fe^{2+}+Mn^{2+}) classification diagram for biotite (Foster 1960). **d** Fe^{3+}-Fe^{2+}-Mg diagram (Wones and Eugster 1965), biotite plotted in the field between the Ni-NiO (NNO) and Fe_2O_3-Fe_3O_4 (HM). **e** Classification diagram of Ti-Fe oxides (Buddington and Lindsley 1964)

and Fe-poor (ESM 9, Fig. 6e) and must be a mixture of ilmenite and fine-grained rutile.

Composition of apatite grains from one diorite and three tonalite porphyry samples at Baogutu were measured to monitor of the sulfate content of the magmas (Parat et al. 2002). The SO_3 contents in apatite with 0.01–0.1-mm-diameter grains are above the detection limit (400 ppm). The apatite from one diorite sample (Fig. 4d) contains high SO_3 (0.17–0.61 wt.%) with an average of 0.28 wt.% (ESM 11, Fig. 7). The apatite from three tonalite porphyry samples (Fig. 4g, h) has a low and variable SO_3 (0.01–0.36 wt.%) with an average 0.13 wt.% (ESM 12, Fig. 7).

Sulfides are mainly chalcopyrite and pyrite, followed by common pyrrhotite and minor arsenopyrite and molybdenite. They are disseminated in diorite and occur in veins. However, some pyrrhotites are primary and interstitial to plagioclase crystals (Fig. 4i, j) and have near stoichiometric compositions (ESM 13 and Fig. 4k).

P-T-H_2O condition of emplacement

Using hornblende composition of the diorite at Baogutu, and based on Ridolfi et al. (2010) and Ridolfi and Renzulli (2012), the crystallization temperature can be calculated, yielding temperatures from 873 to 771 °C with a mean of 812 °C (ESM 4).

At Baogutu, the primary magma of the diorite has a sphene, magnetite, ilmenite, hornblende, biotite, plagioclase, and quartz assemblage. The gases of the fluid included in the hydrothermal alteration stage (Stages 1A–C) are rich in CH_4 and H_2O with minor CO_2, but the dominant gas in the magma stage is H_2O. It is permissive that in the case of the Baogutu samples, the hornblende was in equilibrium with the assemblage biotite-plagioclase-quartz-sphene-Fe-Ti-oxide-melt-(H_2O) vapor (Schmidt 1992), with the exception of orthoclase. The pressures of crystallization at Baogutu are estimated using the Al-in-hornblende geobarometer (Schmidt 1992). Hornblende from main-stage diorite yields pressures

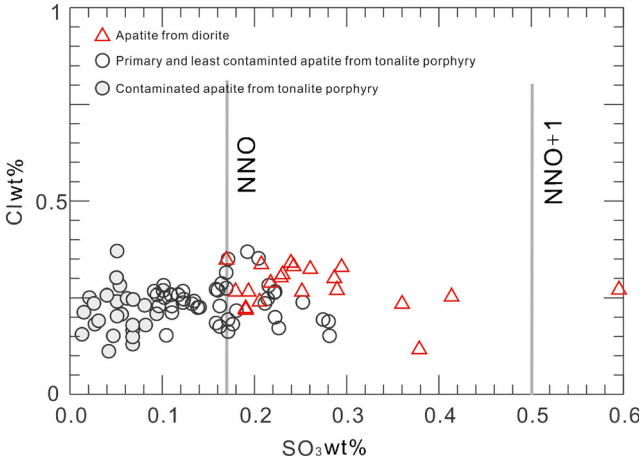

Fig. 7 SO_3 (wt.%) vs. Cl (wt.%) diagrams for the apatite in the diorite (Parat and Holtz 2005)

from 4.2 to 1.8 kbar with an average of 2.5 kbar (ESM 4). The pressure estimates are similar to previous results based on fluid inclusion micro-thermometry (3.1–1.5 kbar; Shen et al. 2010b).

The H_2O content, which depends on the temperature and pressure as well as melt compositions, can be estimated from experimental data (Scaillet and Evans 1999; Klimm et al. 2003; Prouteau and Scaillet 2003). The stability of the amphibole is extremely dependent on the H_2O content of the melt (Scaillet and Evans 1999). Using hornblende composition of diorite at Baogutu, the water content can be calculated based on Ridolfi et al. (2010) and Ridolfi and Renzulli (2012). The water content of the diorite is from 4.86 to 3.37 wt.% with a mean of 4.23 wt.%. This result is also consistent with clinopyroxene in the Baogutu samples.

Diorite is the dominant intrusive rocks of the Baogutu main-stage stock. Therefore, the temperature, pressure, and water content obtained from hornblende in the diorite are considered to be representative of the P-T-H_2O (2.5 kbar, 812 °C, and 4.23 wt.% H_2O) condition of the magma emplacement.

Organic carbon contents of the wall rocks

The organic carbon contents of the wall rocks are from 0.21 to 0.79 % with an average value of 0.45 % and inorganic carbon contents have a wide range from 0.16 to 1.43 % with an average value of 0.51 % (Table 2).

$\delta^{13}C$ of whole rock

The carbon isotopic composition of the whole-rock samples from the Baogutu Group range from −23.1 to −25.8‰ with an average value of −25.0‰ (Table 2).

Gas compositions of fluid inclusions

Our previous work has shown that fluid inclusions from Stages 1B and 1C are rich in CH_4 and H_2O (Shen et al. 2010b). In this study, we determined the gas composition of the fluid inclusions from the magma and late magma stages and the gas compositions of the fluid inclusions from Stages 1B and 1C.

As shown in Fig. 8, in the magma emplacement stage, the gas composition of the fluid inclusions in quartz from the diorite is H_2O-rich with minor CO_2 (Fig. 8a, b). In the magma assimilation stage, the gas composition of the inclusions in quartz from the tonalite porphyry is H_2O-, CO_2-, and CH_4-rich (Fig. 8c, d). In the late magma stage (Stage 1A), fluid inclusions in A-type veins exsolved directly from the magma and were trapped in the one-phase field as supercritical fluids (Richards 2003; Cooke et al. 2005). The gas composition of such inclusions in quartz (Fig. 4k, l) is CH_4- (Fig. 8e) and H_2O-rich (Fig. 8f). In the hydrothermal stage (Stage 1B and 1C), the gas composition of the inclusions in quartz veins is H_2O-, CH_4-, and CO_2-rich (Shen et al. 2010b; Fig. 8g, h).

The gas composition of the inclusions extracted from the Stage 1B and Stage 1C quartz shows that during hydrothermal stage the gas composition of the inclusions is H_2O-, CH_4-, and CO_2-rich (Table 3).

$\delta^{13}C$ of CH_4 and CO_2

The carbon isotopic composition of CH_4 and CO_2 extracted from fluid inclusions in samples from Stages 1B and 1C quartz are listed in Table 3. The $\delta^{13}C$ values of CH_4 and CO_2 vary between −28.2 and −36.0‰ and −6.8 and −20.0 ‰, respectively. There is no correlation between the relative contents and the carbon isotopic composition of CH_4 and CO_2 (Table 3). Although the CH_4 contents of hydrothermal fluids are different in these samples, CH_4 from these samples is isotopically indistinguishable. Using the carbon isotope fractionation factors of Horita (2001), the carbon isotope equilibrium temperature between CH_4 and CO_2 ranges from 294 to 830 °C (Table 2).

Discussion

Origin of CH_4

In most porphyry Cu deposits worldwide, SO_2 and CO_2 have been identified in fluid inclusions, but other gases such as CH_4, H_2S, and N_2 are typically not detected (Rusk and Reed 2002). Our previous and present work has discovered substantial CH_4 in hydrothermal fluids in the Baogutu porphyry Cu deposit. The interesting question is the origin of the abundant CH_4 at Baogutu.

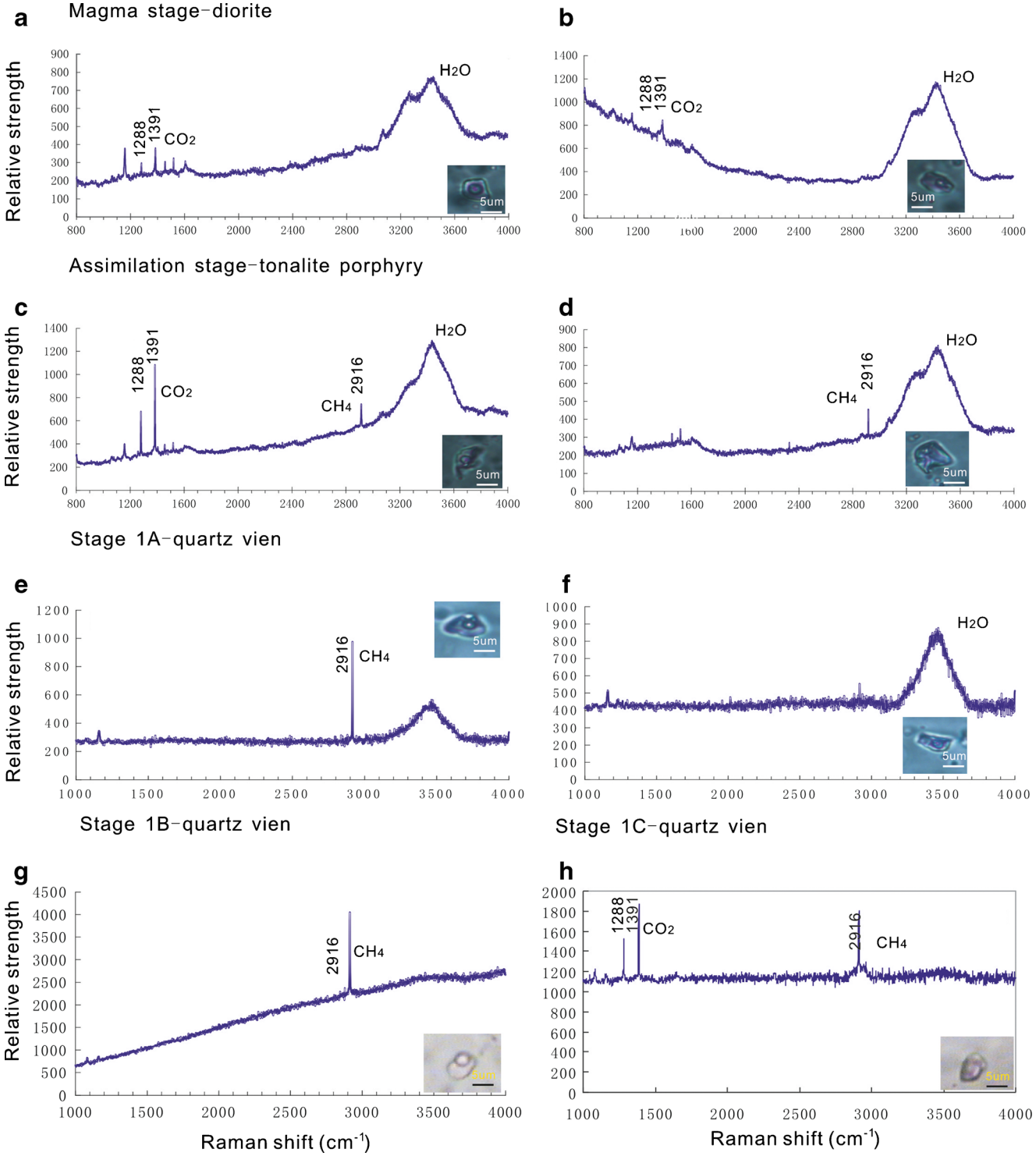

Fig. 8 Laser Raman spectra of fluid inclusions from quartz during the magmatic and hydrothermal stages in the Baogutu deposit. Magma stage—diorite: **a**, **b** spectrum showing the broad water peak and low CO_2 peak. Assimilation stage—tonalite porphyry: **c** spectrum showing the broad water, sharp CO_2 and low CH_4 peaks; **d** spectrum showing the broad water and low CH_4 peaks. Stage 1A—A-type vein: **e** spectrum showing the sharp CH_4 peak; **f** spectrum showing the broad water peak. Stage 1B—quartz veins: **g** spectrum showing the sharp CH_4 peak. Stage 1C—quartz veins: **h** spectrum showing the sharp CO_2 and CH_4 peaks

Geological CH_4 has generally been categorized into three groups (Ueno et al. 2006; Fiebig et al. 2007): microbial (emitted by the metabolic activities of methanogenic microbes), thermogenic (generated by the thermal decomposition of organic matter), and abiogenic [derived from the mantle or produced by non-biological reactions from simple inorganic

compounds (CO_2 and H_2) such as the Fischer–Tropsch-type (FTT) reaction]. We consider these origins in the following sections.

Carbon isotopic composition varies significantly in natural methane. The $\delta^{13}C_{CH4}$ of biogenic methane varies from −66.1 to −69.2‰ (Schoell 1988). $\delta^{13}C_{CH4}$ values of −30 to −20‰ are typical for most thermogenic methanes that occur in continental hydrothermal systems (Giggenbach 1995). Jenden et al. (1993) proposed that one criterion for identification of mantle-derived abiogenic hydrocarbons is a $\delta^{13}C_{CH4}$ value higher than −25‰. In this study, C isotopic composition of CH_4 of fluid inclusions for quartz samples at Baogutu varied from −28.2 to −36.0‰ averaging −31.4‰ (Table 3), suggesting that Baogutu is unlikely of biogenic or mantle-derived abiogenic methane.

The organic carbon contents of wall rocks (Fig. 3d–f) occurred in the Baogutu area are from 0.21 to 0.79 % (Table 2). $\delta^{13}C_{CH4}$ values of −30 to −20‰ are typical for most thermogenic methanes that occur in continental hydrothermal systems (e.g., Panichi et al. 1977; Giggenbach 1995). The $\delta^{13}C_{CH4}$ values (−28.2 to −36.0‰) at Baogutu are compatible with thermogenic CH_4, suggesting that the CH_4 at Baogutu could be a product of thermal decomposition of organic matter from the wall rocks.

If the methane is thermogenic in origin, extracted gas should contain higher hydrocarbons (e.g., ethane and propane) along with methane because thermal decomposition of organic matter yields not only methane but also ethane and propane. The gas composition of the inclusions extracted from the hydrothermal quartz contains minor ethane (Table 3). In addition, thermogenic hydrocarbons derived from thermal degradation of organic matter usually exhibit methane to ethane plus propane ratios smaller than 100 (Fiebig et al. 2009), compatible with the methane to ethane ratios at Baogutu that are from 2 to 70.

As shown in Fig. 9, most CH_4 at Baogutu plots in thermogenic gas field and minor in geothermal gas field. The thermogenic process of CH_4 is related to thermal (>150 °C) degradation of sedimentary organic matter (Whiticar 1999; Bréas et al. 2001). Therefore, it is likely that the CH_4 at Baogutu is produced by the water-rock interactions such as heating of carbonate-bearing wall rocks in situ or in the assimilation process of hot dioritic magma.

The isotopic signature of CO_2 provides further evidence of the carbon-bearing wall rocks' contribution to the ore-forming hydrothermal systems at Baogutu. The $\delta^{13}C_{CH4}$ (−28.2 to −36.0‰) is typical of natural gas generated from sedimentary organic carbon (Giggenbach 1995). The $\delta^{13}C_{CO2}$ (−6.8 to −20.0‰) is typical of that produced by the oxidation of such CH_4 and unlike that derived from Paleozoic marine carbonate rocks (−3 to +3‰; Fiebig et al. 2004). Importantly, $\Delta^{13}C_{CO2\text{-}CH4}$ values (8.2–25‰) indicate carbon isotope equilibrium at elevated temperatures of 294–830 °C in a magmatic hydrothermal system (Table 2). Together, these data suggest that the carbon in hydrothermal fluids was assimilated from a carbonaceous sedimentary source, such as the host Baogutu Group.

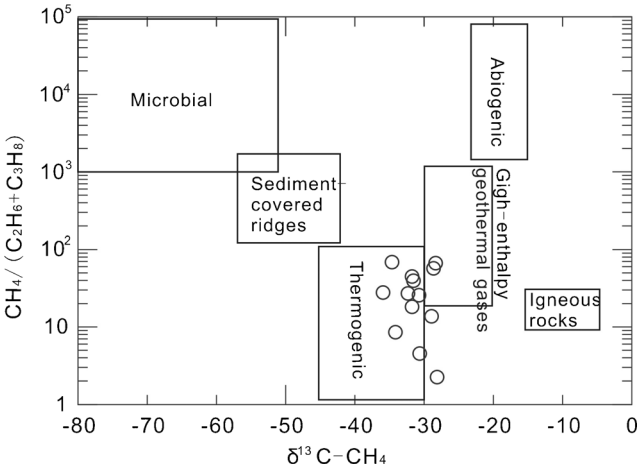

Fig. 9 $CH_4/(C_2H_6+C_3H_8)$ vs. $\delta^{13}C$-CH_4 diagrams for the gases (Cinti et al. 2011; *boxes* are from Hunt 1996)

We must also consider the possibility that non-biological processes such as the FTT reactions (Horita and Berndt 1999; McCollom and Seewald 2001) might have produced the methane. The criteria for identifying methane as abiogenic are ambiguous (Horita and Berndt 1999). One suggested geochemical criterion is $\delta^{13}C_{CH4}$ values higher than −25‰ (Welhan 1988) or between −26 and −9‰ (Ueno et al. 2006). The other criterion is $\delta^{13}C_{CH4}$ values as low as the typically microbial methane (Horita and Berndt 1999). The $\delta^{13}C_{CH4}$ of CH_4 (−28.2 to −36.0‰) at Baogutu is lower than −26‰ and higher than the $\delta^{13}C_{CH4}$ of microbial methane.

If all methane is abiogenic in origin such as the product of the FTT reaction, extracted gas should not contain higher hydrocarbons along with methane, in contrast to the presence of C_2H_6 (Table 3).

FTT reaction enables reasonable chemical and isotopic exchange between dissolved CO_2 and CH_4 at T <500 °C, which is catalyzed by Fe-bearing phases (Giggenbach 1997; Horita and Berndt 1999). Fe(II)-bearing minerals were widespread in the host rocks at Baogutu, but some apparent isotopic temperatures are more than 500 °C, indicating that some CH_4 was not generated from dissolved CO_2 according to FTT reaction. The other apparent isotopic temperatures are between 294 and 500 °C (Table 2). For an evaluation of whether these CO_2 and CH_4 are in chemical equilibrium at magmatic hydrothermal system, $\log(X_{CH4}/X_{CO2})$ ratios of fluids were correlated with corresponding apparent isotopic temperatures in Fig. 10. These measured $\log(X_{CH4}/X_{CO2})$ values plot far away the equilibrium vapor and liquid line defined by the oxygen buffer of Giggenbach (1987) and D'Amore and Panichi (1980). These large deviations suggest that chemical

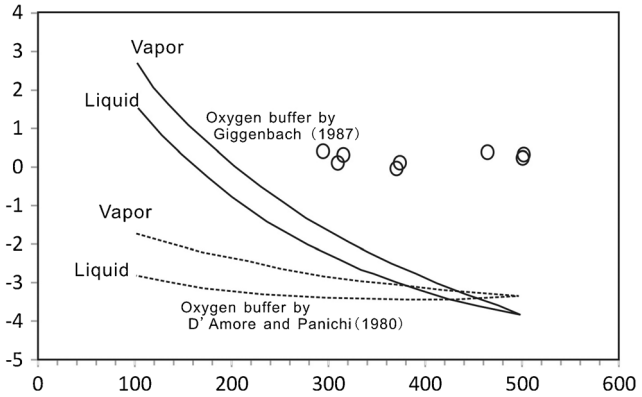

Fig. 10 Correlation between $\log(X_{CH4}/X_{CO2})$ values and apparent isotopic temperatures of the gases (Fiebig et al. 2004). All data points plot far away from the equilibrium liquid lines defined by the semi-empirical oxygen buffers of D'Amore and Panichi (1980) and Giggenbach (1987)

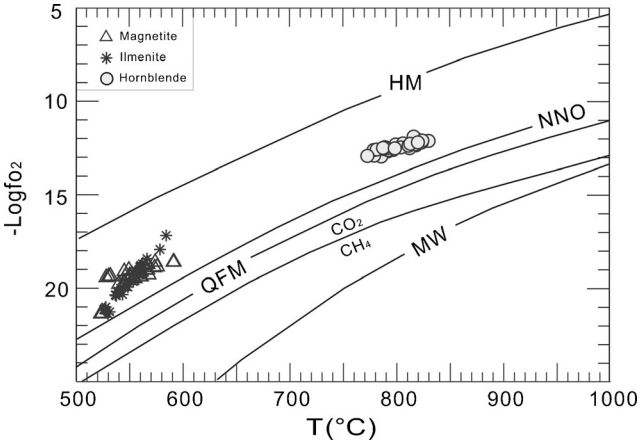

Fig. 11 Oxygen fugacity and temperature diagram. *HM* hematite-magnetite, *NNO* nickel-nickel oxide, *QFM* quartz-fayalite-magnetite (Chou 1987) and CO_2-CH_4 (Candela 1989)

equilibrium between CO_2 and CH_4 was not attained in the hydrothermal system. The abiotic origin of the extracted CH_4 is therefore unlikely.

Magma oxygen fugacity

Primary magma oxygen fugacity

Experimental studies have shown that the Fe/(Fe+Mg) ratio of mafic silicates is a function of fO_2 at fixed temperature (Prouteau and Scaillet 2003). High Mg# values of clinopyroxene (0.58–0.83), hornblende (0.72–0.81), and biotite (0.51–0.61) reflect high fO_2 of the Baogutu magma, similar to other porphyry copper magmas.

As shown in the plot of Fe^{3+}-Fe^{2+}-Mg (Fig. 6d), both primary and hydrothermal biotites plot between Ni-NiO (NNO) and Fe_2O_3-Fe_3O_4 (HM) at FMQ+1 (NNO≈FMQ+0.7; Jugo et al. 2005). Likewise, primary hornblendes plot above NNO or NNO+1 (Fig. 11). Using temperatures from hornblende thermometry, the calculated fO_2 is from −11.15 to −12.93 (ESM 4).

The gas composition of fluid inclusions in quartz from the diorites contains dominant H_2O with minor CO_2 and lacks CH_4 (Fig. 8a, b). Apatite from diorite is sulfur-rich and has high and variable SO_3 (0.17–0.61 wt.%) with an average of 0.28 wt.% (ESM 11). As shown in Fig. 7, most data plot between NNO and NNO+1. The presence of SO_3 in apatite from Baogutu indicates that at least some S in the melt was oxidized (S^{6+}) (Streck and Dilles 1998).

Based on these results, we infer that the diorite magma was oxidized and estimate its redox conditions at $\log fO_2$>NNO or FMQ+1 with dominant Mg-hornblende, Mg-biotite, and minor magnetite, ilmenite, and sphene assemblages and H_2O and minor CO_2 vapor. The oxygen fugacity is near to the previously recognized lower limit of most copper porphyries (FMQ+2; Mungall 2002).

Contaminated magma oxygen fugacity

Temperatures and pressures estimated from hornblende in the Baogutu diorite are T=812 °C and P=2.5 kbar during the magma crystallization process (ESM 4). Temperatures estimated from magnetite-ilmenite pairs indicate equilibrium temperatures under the sub-solidus condition from 524 to 574 °C (ESMs 7, 8). The calculated *T-P* implies that the magmas were emplaced at moderated depths and would have cooled slowly. This magmatic condition could have caused partial melting of adjacent country rocks and assimilation in the magma.

At Baogutu, the greatest amount of contamination occurred during crystallization of the tonalite porphyry (Shen and Pan 2013). The tonalite porphyry contains two (space)-type of apatite: (1) primary or least contaminated apatite, generated by the crystallization of magma almost without country rock; and (2) contaminated apatite, generated by the assimilation-contamination of country rock during crystallization of the magma. The primary apatite is homogeneous and similar to the apatite of the diorite (Fig. 4d), whereas the contaminated apatite is heterogeneous (Fig. 4g, h). The primary apatite is sulfur-rich and high and variable SO_3 (0.09–0.28 wt.%) with an average of 0.17 wt.% (ESM 12). The SO_3 contents are near to NNO (Fig. 7). The contaminated apatite is sulfur-poor and has a low SO_3 (0.01–0.10 wt.%) with an average of 0.05 wt.% (ESM 12). The SO_3 contents are below NNO (Fig. 7). The gas composition of fluid inclusions in quartz from the tonalite porphyry is both CO_2- and CH_4-rich (Fig. 8c, d). This indicates that the oxygen fugacity of the tonalite porphyry magma is therefore lower than that of the primary diorite magma.

Fluid oxygen fugacity

Exsolved fluid oxygen fugacity

Stage 1A Ca-Na silicate alteration assemblages, A-type veins (Fig. 4k, l), and interstitial pyrrhotite (Fig. 4i, j) are closely related in time and space to the emplacement of the main-stage diorite stock. The fluid trapping condition is at T>400 °C and P=1500 to 3100 bar in the transitional stage (Stage 1A) from magma to the hydrothermal stage (Shen et al. 2010a, b). The pressure and temperature of this early type of alteration and veining were close to that of the final crystallization of the melt itself. The pressure is clearly greater than hydrostatic pressure. Possible sources of aqueous fluid in Stage 1A are the melt itself or meteoric water from surrounding host rocks. Meteoric water is not a likely source for the simple reason that it could not migrate into the high-pressure region where Stage 1A alteration at Baogutu was accomplished.

At Baogutu, fluid inclusions in quartz from the A-type veins are CH_4- (Fig. 8e) and H_2O-rich (Fig. 8f). The fluid oxygen fugacity is approximately equal to the FMQ buffer in the CH_4-H_2O-graphite region (Holloway 1984). Under reducing conditions (fO_2<FMQ), sulfur is dissolved predominantly as S^{2-} in silicate melts (Matthews et al. 1999; Jugo et al. 2005) and pyrrhotite could be crystallized from mono-sulfide solid solution (Whitney 1984). At Baogutu, the presence of pyrrhotite and lack of pyrrhotite-chalcopyrite association suggest very low oxygen fugacity of fluids. Thus, the fluid oxygen fugacity in Stage 1A at Baogutu could be close to or below the FMQ buffer. It is much lower than that of the primary diorite magma at Baogutu. It is also clearly lower than that of the supercritical fluids in most porphyry Cu deposits worldwide which could form abundant magnetite, hematite, and anhydrite. In addition, the Stage 1A at Baogutu is barren of Cu, Au, and Mo. It is also different from some porphyry Cu deposits in which the supercritical fluid stage is the mineralization stage with pyrrhotite-chalcopyrite association, such as El Salvador, Chile (Gustafson and Quiroga 1995).

Hydrothermal fluid oxygen fugacity

As consolidation and cooling of the Baogutu intrusive complex progressed, the structural and chemical character of the accompanying alteration and mineralization shifted. Barren discontinuous and irregular veining gave way to mineralized continuous veins and the Ca-Na silicate alteration evolved into potassic and phyllic alteration.

Magnetite is common in potassic alteration, but ilmenite is rare in the main ore genesis stage of the porphyry copper deposits all over the world. At Baogutu, chalcopyrite, rutile, ilmenite, and sphene occurred in the potassic alteration zone (Fig. 5a–c). No high fO_2 minerals occur in fluid inclusions hosted in mineralized quartz veinlets in the biotite zone (Shen et al. 2010a, b). On the contrary, CH_4 gas in these fluid inclusions (Table 3) suggests that the fluid fO_2 in Stage 1B could be near to the FMQ buffer.

At Baogutu, there was more CO_2 in the hydrothermal fluids of the phyllic stage (Fig. 8h). The transfer of CO_2 to the vapor in the fluids can be explained by the changes in alteration style from potassic to phyllic. This is supported by the fact of the oxidation of CH_4 to CO_2 and H_2O by chloritization of biotite (Fig. 5d, e) during the phyllic stage (Tarantola et al. 2009).

$$CH_4 + 2O_2 \rightarrow CO_2 + 2H_2O \quad (1)$$

$$12\,Fe_2O_3(\text{biotite}) \rightarrow 8\,Fe_3O_4(\text{chlorite}) + 2O_2 \quad (2)$$

$$CH_4 + 12\,Fe_2O_3(\text{biotite}) \rightarrow CO_2 + 8\,Fe_3O_4(\text{chlorite}) + 2H_2O \quad (3)$$

In the phyllic stage (Stage 1C), the sericite alteration is widespread and the pH was lower than neutral. Thus, the phyllic alteration assemblages, mineralized veins with chalcopyrite, pyrite, and molybdenite (Fig. 5f), and the H_2O-CO_2-CH_4 system suggest that the fluid oxygen fugacity in Stage 1C above the FMQ buffer.

Evolution of the magmatic-hydrothermal system

The main-stage stock at Baogutu underwent magma crystallization, magma and country-rock assimilation-contamination, Ca-Na silicate (Stage 1A), potassic (Stage 1B), and phyllic (Stage 1C) alteration stages. In the magmatic stage, ore-bearing magmas have been generated as oxidized partial melts in subduction zones (Shen et al. 2009), with subsequent ascent and emplacement in the West Junggar terrain (Fig. 12a). The magma was under the oxidation states (>NNO) with Mg-hornblende, Mg-biotite, magnetite, sphene, and ilmenite assemblages. Under oxidizing conditions, sulfur is dissolved mostly as S^{6+} in silicate melts (Matthews et al. 1999; Jugo et al. 2005). Therefore, the chalcophile elements in magma behave incompatibly and they can be partitioned into the supercritical fluid. As a consequence, chalcophile elements at Baogutu should be exsolved from the magma chamber and dissolved in the fluids. The Baogutu dioritic magma was emplaced at about 800 °C and at 8 km deep (Fig.12a), and it assimilated surrounding felsic, carbon-bearing wall rocks prior to mineralization (Fig. 12b). This caused the wall rocks heated by hot dioritic to melt and continuously produce CH_4.

In Stage 1A, the fluids exsolved from the magma chamber at depth were channeled upwards along faults into the Baogutu main-stage stock. The CH_4 gas derived from the wall

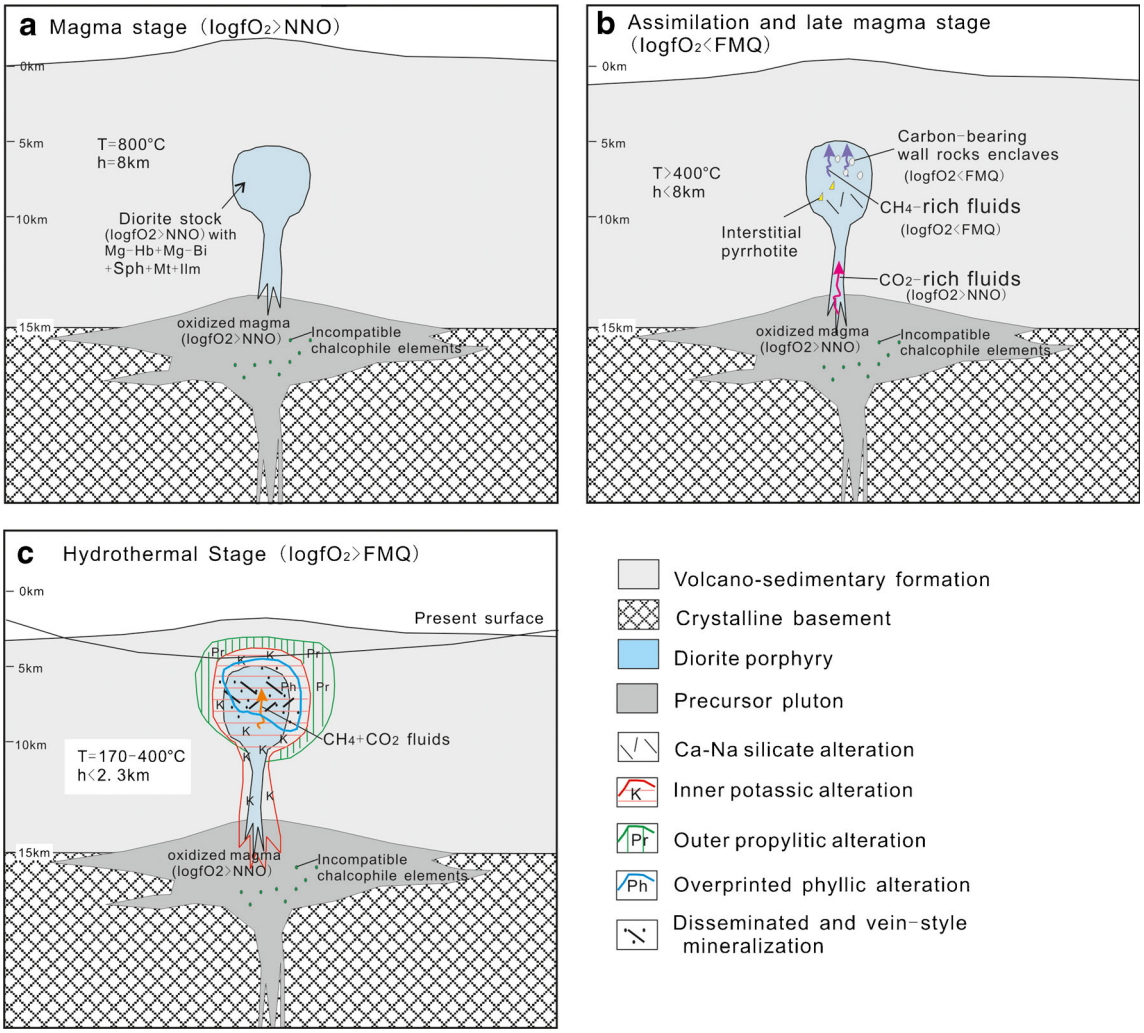

Fig. 12 Schematic cross-section through the Baogutu porphyry copper forming system. **a** Magma stage ($\log fO_2$>FMQ+1): upper crustal batholith complex of basaltic-andesitic composition under oxidized condition includes incompatible chalcophile elements retained in the magmatic hydrothermal fluids. After further fractionation at this level, evolved, volatile-rich andesitic magmas are emplaced at shallow levels. **b** Assimilation stage and late-magma stage ($\log fO_2$<FMQ): diorite assimilates carbon-bearing wall rocks and CH_4-rich hydrothermal fluids and forms magmatic pyrrhotite. **c** Hydrothermal stage ($\log fO_2$>FMQ): CH_4-CO_2 fluids interact with the diorite and produce potassic and propylitic zones overprinted by phyllic alteration

rocks was incorporated into the exsolved fluids. This can reduce SO_4^{2-} to H_2S, ferric to ferrous iron, and consequently promotes pyrrhotite crystallization and inhibits anhydrite and magnetite precipitation (Fig. 12b). Fluid oxygen fugacity is below the FMQ buffer and is much lower than that of the primary magma.

In the hydrothermal stage (Stage 1B and 1C), the CH_4-CO_2 fluids interacted with the diorite and produced the potassic alteration, characterized by rutile, sphene, and relict ilmenite rather than secondary magnetite. The evolution of alteration from potassic to phyllic resulted in the transfer of CO_2 to the vapor in the fluids and to form the CO_2-CH_4 fluids forming dominant disseminated and minor vein mineralization (Fig. 12c). The fluid oxygen fugacity is above the FMQ buffer.

Comparison with classic porphyry Cu deposits

Classic porphyry copper deposits are characterized by abundant primary high fO_2 minerals (magnetite, hematite, and anhydrite) in equilibrium with hypogene copper-iron sulfide minerals (chalcopyrite, bornite) and have fluid inclusions with CO_2>>CH_4 that are indicative of high fO_2. The Baogutu data suggest that the dioritic magma initially was oxidized, but was then reduced by the assimilation-contamination of the carbon-bearing wall rocks forming the CH_4-rich fluids.

1. The Baogutu diorite is characterized by primary magnetite and ilmenite assemblage rather than the magnetite, hematite, and anhydrite assemblage. Baogutu dioritic magma initially was oxidized (>FMQ+1), but its

oxidation states may be lower than the states of most porphyry magmas (>FMQ+2; Mungall 2002).

2. During the magma crystallization process, the temperature (T=812 °C) and pressure (P=2.5 kbar) of the Baogutu diorite were higher than the P-T conditions of most porphyry magmas. The magmatic conditions could have caused partial melting and assimilation-contamination of adjacent country rocks.
3. The decreases in oxygen fugacity coincide with abundant reduced CH_4 gas formation and pyrrhotite crystallization. The occurrences of magmatic sulfides at Baogutu are different from those of porphyry deposits. The latter are dissolved and entrained into a magmatic chamber; they may act as a temporary storage medium for the ore metals (i.e., Halter 2005; Audétat et al. 2008).
4. Classic porphyry Cu deposits have a gradually decreasing fO_2 from magma to hydrothermal stages. High fO_2 destroys sulfide in the source region and keeps the melt sulfide under-saturated, thereby promoting porphyry copper mineralization. The Baogutu porphyry Cu deposits had a fluctuating fO_2 which changes from high fO_2 magma, through very low fO_2 supercritical fluid, to a moderate fO_2 hydrothermal fluid. The carbon contamination is essential for the fO_2 fluctuation.

Conclusions

1. Although the Baogutu porphyry Cu deposit is characterized by considerable amounts of CH_4 in hydrothermal fluids, its primary host, dioritic magma, is an oxidized magma.
2. The host diorite underwent the carbon-bearing country-rock contamination. The CH_4 ($\delta^{13}C_{VPDB}$=−28.2 to −36.0‰) is thermogenic CH_4 which is generated by the thermal decomposition of organic matter from country rock.
3. The dioritic magma was reduced by country-rock contamination, which has played an important role in the decreasing fO_2 of the supercritical fluids exsolved from them. The sharply decreasing redox potential of the fluid is the key to, and a direct cause of, the formation of the reduced porphyry Cu deposit.
4. The fO_2 of the magmatic hydrothermal system is variable. The evolution sequence is magmatic stage ($\log fO_2$>FMQ+1) with primary magnetite, sphene, and ilmenite→assimilation-contamination and late magma stage ($\log fO_2$<FMQ) with CH_4-rich fluids and primary pyrrhotite→hydrothermal stage ($\log fO_2$>FMQ) with CH_4-CO_2 fluids, relict ilmenite, and mineralized quartz-sulfide.

Acknowledgments We are very grateful to Editor-in-chief Georges Beaudoin, associate editor T. Wagner, and two reviewers for constructive comments and improvement of the manuscript. Editor-in-chief Georges Beaudoin and one reviewer have also carefully provided detailed corrections which substantially improved the presentation. We are indebted to H.P. Zhu for help during the gas compositions analysis, Q. Mao for help during the mineral composition analysis, and L.J. Feng for help during the carbon isotope analysis. This paper was financially supported by the National Natural Science Foundation of China (Grant No. U1303293, 41390442, 41272109, 40972064), Key Deployment Project of the Chinese Academy of Sciences (Grant No. KJZD-EW-TZ-G07), National International Cooperation in Science and Technology Project (Grant No. 2010DFB23390), and National 305 Project (Grant No. 2011BAB06B01).

References

Ague JJ, Brimhall GH (1988) Magmatic arc asymmetry and distribution of anomalous plutonic belts in the batholiths of California: effects of assimilation, crustal thickness, and depth of crystallization. Geol Soc Am Bull 100:912–927

Audétat A, Pettke T, Heinrich CA, Bodnar RJ (2008) The composition of magmatic-hydrothermal fluids in barren and mineralized intrusions. Econ Geol 103:877–908

Bréas O, Guillou C, Reniero F, Wada E (2001) The global methane cycle: isotopes and mixing ratios, sources and sinks. Isot Environ Health Stud 37:257–379

Buddington AF, Lindsley DH (1964) Iron-titanium oxide minerals and synthetic equivalents. J Petrol 5:310–357

Burke EA (2001) Raman microspectrometry of fluid inclusions. Lithos 55:139–158

Candela PA (1989) Felsic magmas, volatiles, and metallogenesis. In: Whitney JA, Naldrett AJ (eds) Ore deposition associated with magmas. Rev Econ Geol 4:223–233

Chou IM (1987) Oxygen buffer and hydrogen sensor techniques at elevated pressures and temperatures. In: Ulmer GC, Barnes HL (eds) Hydrothermal experimental techniques. John Wiley, Chichester, pp 61–99

Cinti D, Procesi M, Tassi F, Montegrossi G, Sciarra A, Vaselli O, Quattrocchi F (2011) Fluid geochemistry and geothermometry in the western sector of the Sabatini Volcanic District and the Tolfa mountains (central Italy). Chem Geol 284:160–181

Cooke DR, Hollings P, Walshe JL (2005) Giant porphyry deposits: characteristics, distribution, and tectonic controls. Econ Geol 100:801–818

D'Amore F, Panichi C (1980) Evaluation of deep temperature of hydrothermal systems by a new gas geothermometer. Geochim Cosmochim Acta 44:549–556

Dilles JH, Einaudi MT (1992) Wall-rock alteration and hydrothermal flow paths about the Ann-Mason porphyry copper deposit, Nevada: a 6-km vertical reconstruction. Econ Geol 87:1963–2001

Fiebig J, Chiodini G, Caliro S, Rizzo A, Spangenberg J, Hunziker JC (2004) Chemical and isotopic equilibrium between CO_2 and CH_4 in fumarolic gas discharges: generation of CH_4 in arc magmatic-hydrothermal systems. Geochim Cosmochim Acta 68:2321–2334

Fiebig J, Woodland AB, Alessandro WD, Püttmann W (2009) Excess methane in continental hydrothermal emissions is abiogenic. Geology 37:495–498

Fiebig J, Woodland AB, Spangenberg J, Oschmann W (2007) Natural evidence for rapid abiogenic hydrothermal generation of CH_4. Geochim Cosmochim Acta 71:3028–3039

Foster MD (1960) Interpretation of the composition of trioctahedral micas. U S Geol Surv Prof Pap 354B:11–49

Giggenbach WF (1987) Redox processes governing the chemistry of fumarolic gas discharges from White Island, New Zealand. Appl Geochem 2:143–161

Giggenbach WF (1995) Variations in the chemical and isotopic composition of fluids discharged from the Taupo Volcanic Zone, New Zealand. J Volcanol Geotherm Res 68:89–116

Giggenbach WF (1997) Relative importance of thermodynamic and kinetic processes in governing the chemical and isotopic composition of carbon gases in high-heatflow sedimentary systems. Geochim Cosmochim Acta 61:3763–3785

Gustafson LB, Hunt JP (1975) The porphyry copper deposit at El Salvador, Chile. Econ Geol 70:857–912

Gustafson LB, Quiroga J (1995) Patterns of mineralization and alteration below the porphyry copper orebody at El Salvador, Chile. Econ Geol 90:2–16

Halter (2005) Magma evolution and the formation of porphyry Cu-Au ore fluids: evidence from silicate and sulfide melt inclusions. Miner Depos 39:845–863

Hedenquist JW, Lowenstern JB (1994) The role of magmas in the formation of hydrothermal ore deposits. Nature 370:519–527

Holloway JR (1984) Graphite–CH_4–H_2O–CO_2 equilibria at low grade metamorphic conditions. Geology 12:455–458

Horita J (2001) Carbon isotope exchange in the system CO_2-CH_4 at elevated temperatures. Geochim Cosmochim Acta 65:1907–1919

Horita J, Berndt ME (1999) Abiogenic methane formation and isotopic fractionation under hydrothermal conditions. Science 285:1055–1057

Hunt JM (1996) Petroleum geochemistry and geology. W.H. Freeman and Company, New York

Jenden PD, Hilton DR, Kaplan IR, Craig H (1993) Abiogenic hydrocarbons and mantle helium in oil and gas fields. In: Howell DG (ed) The future of energy gases—USGS Professional Paper 1570. United States Geological Survey, Washington, DC, pp 57–82

Jugo P, Luth R, Richards J (2005) Experimental data on the speciation of sulfur as a function of oxygen fugacity in basaltic melts. Geochim Cosmochim Acta 69:497–503

Kirkham RV, Sinclair WD (1995) Porphyry copper, gold, molybdenum, tungsten, tin, silver. In: Eckstrand OR, Sinclair WD, Thorpe RI (eds) Geology of Canadian mineral deposit types: geological survey of Canada, Geology of Canada 8:421–446

Klimm K, Holtz F, Johannes W, King PL (2003) Fractionation of metaluminous A-type granites: an experimental study of the Wangrah Suite, Lachlan Fold Belt, Australia. Precambrian Res 124:327–341

Leake BE (1997) Nomenclature of amphiboles: report of the Subcommittee on Amphiboles of the International Mineralogical Association Commission on New Minerals and Mineral Names. Mineral Mag 61:295–321

Li HW, Feng LJ, Li TJ, Chen J, Liu W (2014) Combination of sealed-tube decrepitation with continuous-flow isotope ratio mass spectrometry for carbon isotope analyses of CO_2 from fluid inclusions in minerals. Anal Methods 6:4504–4506

Matthews SJ, Moncrieff DHD, Carroll MR (1999) Empirical calibration of the sulphur valence oxygen barometer from natural and experimental glasses: method and applications. Mineral Mag 63:421–431

McCollom TM, Seewald JS (2001) A reassessment of the potential for reduction of dissolved CO_2 to hydrocarbons during serpentinization of olivine. Geochim Cosmochim Acta 65:3769–3778

Morimoto N, Fabries J, Ferguson AK, Ginzburg IV, Ross M, Seifert FA, Zussman J, Aoki K, Gottardi G (1988) Nomenclature of pyroxenes. Am Mineral 73:1123–1133

Mungall JE (2002) Roasting the mantle: slab melting and the genesis of major Au and Au-rich Cu deposits. Geology 30:915–918

Panichi C, Ferrara GC, Gonfiantini R (1977) Isotope geothermometry in the Larderello geothermal field. Geothermics 5:81–88

Parat F, Holtz F (2005) Sulfur partition coefficient between apatite and rhyolite: the role of bulk S content. Contrib Mineral Petrol 150:643–651

Parat F, Dungan MA, Streck MJ (2002) Anhydrite, pyrrhotite and sulfur-rich apatite: tracing the sulfur evolution of an Oligocene andesite (Eagle Mountain, CL, USA). Lithos 64:63–75

Prouteau G, Scaillet B (2003) Experimental constraints on the origin of the 1991 Pinatubo dacite. J Petrol 44:2203–2241

Rabbia OM, Hernández LB, French DH, King RW, Ayers JC (2009) The El Teniente porphyry Cu-Mo deposit from a hydrothermal rutile perspective. Mineral Deposita 44:849–866

Richards JP (2003) Tectono-magmatic precursors for porphyry Cu-(Mo-Au) deposit formation. Econ Geol 98:1515–1533

Ridolfi F, Renzulli A (2012) Calcic amphiboles in calc-alkaline and alkaline magmas: thermobarometric and chemometric empirical equations valid up to 1,130°C and 2.2 GPa. Contrib Mineral Petrol 163:877–895

Ridolfi F, Renzulli A, Puerini M (2010) Stability and chemical equilibrium of amphibole in calc-alkaline magmas: an overview, new thermobarometric formulations and application to subduction-related volcanoes. Contrib Mineral Petrol 160:45–66

Rowins SM (1999) Reduced porphyry copper-gold deposits: a newly recognized style of gold mineralization. Geol Soc Am Abstr Programs 31(7):A-92

Rowins SM (2000) Reduced porphyry copper-gold deposits: a new variation on an old theme. Geology 28:491–494

Rusk B, Reed M (2002) Scanning electron microscope-cathodoluminescence analysis of quartz reveals complex growth histories in veins from the Butte porphyry copper deposit, Montana. Geology 30:727–730

Scaillet B, Evans BW (1999) The 15 June 1991 eruption of Mount Pinatubo. I. Phase equilibria and pre-eruption P–T–fO_2–fH_2O conditions of the dacite magma. J Petrol 40:381–411

Schmidt MW (1992) Amphibole composition in tonalite as a function of pressure: an experimental calibration of the Al-in-hornblende barometer. Contrib Mineral Petrol 110:304–310

Schoell M (1988) Multiple origins of methane in the Earth. Chem Geol 71:1–10

Shen P, Pan HD (2013) Country-rock contamination of magmas associated with the Baogutu porphyry Cu deposit, Xinjiang, China. Lithos 177:451–469

Shen P, Shen YC, Liu TB, Meng L, Dai HW, Yang YH (2009) Geochemical signature of porphyries in the Baogutu porphyry copper belt, western Junggar, NW China. Gondwana Res 16:227–242

Shen P, Shen YC, Pan HD, Wang JB, Zhang R, Zhang YX (2010a) Baogutu porphyry Cu-Mo-Au deposit, West Junggar, Northwest China: petrology, alteration, and mineralization. Econ Geol 105:947–970

Shen P, Shen YC, Wang JB, Zhu HP, Wang LJ, Meng L (2010b) Methane-rich fluid evolution of the Baogutu porphyry Cu-Mo-Au deposit, Xinjiang, NW China. Chem Geol 275:78–98

Shen P, Shen YC, Pan HD (2011) Character of the reduced porphyry Cu deposits in western Junggar. International workshop on the large Balkash-western Junggar copper-gold province. 75–80

Shen P, Shen YC, Li XH, Pan HD, Zhu HP, Meng L (2012a) Northwestern Junggar Basin, Xiemisitai Mountains, China: a geochemical and geochronological approach. Lithos 140–141:103–118

Shen P, Shen YC, Pan HD, Li XH, Dong LH, Wang JB, Zhu HP, Dai HW, Guan WN (2012b) Geochronology and isotope geochemistry of the Baogutu porphyry copper deposit in the West Junggar region, Xinjiang, China. J Asian Earth Sci 49:99–115

Shen P, Pan HD, Xiao WJ, Li XH, Dai HW, Zhu HP (2013) Early Carboniferous intra-oceanic arc and back-arc basin system in the West Junggar, NW China. Int Geol Rev 55:1991–2007

Shen P, Pan HD, Xiao WJ, Shen YC (2014) An Ordovician intra-oceanic subduction system influenced by ridge subduction in the West Junggar, Northwest China. Int Geol Rev 56(2):206–223

Sillitoe RH (2010) Porphyry copper systems. Econ Geol 105:3–41

Smith CM, Canil D, Rowins SM, Friedman R (2012) Reduced granitic magmas in an arc setting: the Catface porphyry Cu–Mo deposit of the Paleogene Cascade Arc. Lithos 154:361–373

Song HX, Liu YL, Qu WJ, Song B, Zhang R, Cheng Y (2007) Geological characters of Baogutu porphyry copper deposit in Xinjiang, NW China. Acta Petrol Sin 23:1891–1988 (in Chinese with English abstract)

Streck MJ, Dilles JH (1998) Sulfur evolution of oxidized arc magmas as recorded in apatite from a porphyry copper batholith. Geology 26(6):523–526

Tarantola A, Mullis J, Guillaume D, Dubessy J, de Capitani C, Abdelmoula M (2009) Oxidation of CH_4 to CO_2 and H_2O by chloritization of detrital biotite at 270±5 °C in the external part of the Central Alps, Switzerland. Lithos 112:497–510

Ueno Y, Yamada K, Yoshida N, Maruyama S, Isozaki Y (2006) Evidence from fluid inclusions for microbial methanogenesis in the early Archaean era. Nature 440:516–519

Welhan JA (1988) Origins of methane in hydrothermal systems. Chem Geol 71:183–198

Whiticar MJ (1999) Carbon and hydrogen isotope systematics of bacterial formation and oxidation of methane. Chem Geol 161:291–314

Whitney JA (1984) Volatiles in magmatic systems. In: Henley RW, et al., (eds) Fluid-mineral equilibria in hydrothermal systems. Rev Econ Geol 1:155–175

Wones DR, Eugster HP (1965) Stability of biotite—experiment theory and application. Am Mineral 50:1228–1272

Xiao WJ, Han CM, Yuan C, Sun M, Lin SF, Chen HL, Li ZL, Li JL, Sun S (2008) Middle Cambrian to Permian subduction-related accretionary orogenesis of Northern Xinjiang, NW China: implications for the tectonic evolution of central Asia. J Asian Earth Sci 32:102–117

Zhu HP, Wang LJ (2000) Determining gaseous composition of fluid inclusions with Quadrupole Mass Spectrometer. Sci China D 31:586–590 (in Chinese)

Zhu MT, Wu G, Xie HJ, Liu J, Mei M (2012) Geochronology and fluid inclusion studies of the Lailisigaoer and Lamasu porphyry–skarn Cu–Mo deposits in Northwestern Tianshan, China. J Asian Earth Sci 49:116–130